and intractableness of tumors in advanced stages,[33] the presence of subpopulations with a high invasive potential (termed "budding") characterizes tumor heterogeneity in CRCs.[19,20] Budding is defined as detachment from tumor tissues into single or up to five cancer cell clusters at invasive front lesions of CRCs.[19,20] Previous reports, including our own, indicate that tumor budding undergoes EMT.[34–36] The clinical guidelines of the European Society for Medical Oncology[37] and the Japanese Society for Cancer of the Colon and Rectum[38] include tumor budding. Based on these backgrounds, we aimed to examine the glycolytic characteristics of the deepest part of tumor and those of the cancer cells undergoing EMT in this study.

According to the previous studies, the association between HK2 and RFS has not been clear and consistent results could not be acquired yet.[39–43] A possible explanation for this controversy is that the samples analyzed in these studies might be obtained from the superficial tissues of tumor. In considering the role of HK2 in aerobic glycolysis in the invasive front lesions of CRCs, where the cancer cells are usually located in the deep parts of tumors and are stimulated to invade and metastasize, the present study focused on samples from the invasive front lesions of CRCs. The present study showed that enhanced glucose uptake and glycolysis in the deeper parts of the tumor was associated with tumor growth and invasion, as shown by the data of lymph node metastasis samples. Thus, in invasive fronts, our results suggest that cancer metabolism may be reprogrammed and dominantly shifted toward active glycolysis.

We also studied the expression of p-PDH. Considering that p-PDH is involved in the OxPhos inhibition in the mitochondria and contributes to the establishment of aerobic glycolysis, it is possible that high p-PDH is associated with poor prognosis. Contrary to this original expectation, the present analysis of the invasive fronts of CRCs showed that low p-PDH was associated with poor prognosis, and evaluation of combined expression of p-PDH and HK2 demonstrated a clear association with patient prognosis. The results suggest that p-PDH plays a unique role in the malignant behavior of CRCs. Interestingly, recent studies have identified two subpopulations of cancer cells that are distinct in their energy-generating pathways.[44–46] One subpopulation depends on anaerobic glycolysis and secretes massive lactate. The other subpopulation can use lactate from upstream glycolysis in individual cells as well as from surrounding cells, and therefore the metabolites produced by the abovementioned subpopulation. The latter subpopulation can use lactate as the energy source by employing OxPhos in the mitochondria.[46] Also as suggested by our *in vitro* experiments, we speculate that CRC cells perform OxPhos in invasive front lesions. This hypothesis may be further supported by the observations that the citric cycle generates reactive oxygen species by OxPhos, which promote EMT and further cancer invasion.[47] Assessment of combined expression of HK2 and p-PDH may be useful for detecting highly malignant CRC cells. Further investigation should be performed via more detailed mechanistic studies of cancer metabolism associated with invasion and budding to identify more accurate predictors of patient prognosis and to regulate cancer invasion and metastasis.

In conclusion, combined expression of HK2 and p-PDH, as a novel cancer metabolomics-associated biomarker measure, may be clinically useful for predicting tumor aggressiveness and survival in CRC.

Acknowledgments

We thank the members of our laboratories for their helpful discussions. This work was supported in part by a Grant-in-Aid for Scientific Research from the Ministry of Education, Culture, Sports, Science, and Technology; a Grant-in-Aid from the Third Comprehensive 10-year Strategy for Cancer Control, Ministry of Health, Labor, and Welfare; a grant from the Kobayashi Cancer Research Foundation; a grant from the Princess Takamatsu Cancer Research Fund, Japan; a grant from the National Institute of Biomedical Innovation; and a grant from the Osaka University Drug Discovery Funds.

Disclosure Statement

A.H. is a research fellow of the Japan Society for the Promotion of Science. M.K., N.N., J.K., M.M., and H.I. received partial support from Chugai Co., Ltd., Yakult Honsha Co., Ltd., Merck Co., Ltd., Taiho Pharmaceutical Co., Ltd., Takeda Science Foundation and Takeda Medical Research Foundation through institutional endowments.

References

1 Jemal A, Bray F, Center MM, Ferlay J, Ward E, Forman D. Global cancer statistics. *CA Cancer J Clin* 2011; **61**: 69–90.
2 Vaiopoulos AG, Athanasoula KC, Papavassiliou AG. Epigenetic modifications in colorectal cancer: molecular insights and therapeutic challenges. *Biochim Biophys Acta* 2014; **1842**: 971–80.
3 Ribelles N, Santonja A, Pajares B, Llacer C, Alba E. The seed and soil hypothesis revisited: current state of knowledge of inherited genes on prognosis in breast cancer. *Cancer Treat Rev* 2014; **40**: 293–9.
4 Levine AJ, Puzio-Kuter AM. The control of the metabolic switch in cancers by oncogenes and tumor suppressor genes. *Science* 2010; **330**: 1340–4.
5 Kroemer G, Pouyssegur J. Tumor cell metabolism: cancer's Achilles' heel. *Cancer Cell* 2008; **13**: 472–82.
6 Warburg O. On the origin of cancer cells. *Science* 1956; **123**: 309–14.
7 Christofk HR, Vander Heiden MG, Harris MH *et al.* The M2 splice isoform of pyruvate kinase is important for cancer metabolism and tumour growth. *Nature* 2008; **452**: 230–3.
8 Yi W, Clark PM, Mason DE *et al.* Phosphofructokinase 1 glycosylation regulates cell growth and metabolism. *Science* 2012; **337**: 975–80.
9 Patra KC, Wang Q, Bhaskar PT *et al.* Hexokinase 2 is required for tumor initiation and maintenance and its systemic deletion is therapeutic in mouse models of cancer. *Cancer Cell* 2013; **24**: 213–28.
10 Fan J, Shan C, Kang HB *et al.* Tyr Phosphorylation of PDP1 toggles recruitment between ACAT1 and SIRT3 to regulate the pyruvate dehydrogenase complex. *Mol Cell* 2014; **20**: 534–48.
11 Robey RB, Hay N. Mitochondrial hexokinases, novel mediators of the antiapoptotic effects of growth factors and Akt. *Oncogene* 2006; **25**: 4683–96.
12 Wilson JE. Isozymes of mammalian hexokinase: structure, subcellular localization and metabolic function. *J Exp Biol* 2003; **206**: 2049–57.
13 Mathupala SP, Rempel A, Pedersen PL. Glucose catabolism in cancer cells: identification and characterization of a marked activation response of the type II hexokinase gene to hypoxic conditions. *J Biol Chem* 2001; **276**: 43407–12.
14 Kolobova E, Tuganova A, Boulatnikov I, Popov KM. Regulation of pyruvate dehydrogenase activity through phosphorylation at multiple sites. *Biochem J* 2001; **358**: 69–77.
15 Roche TE, Baker JC, Yan X *et al.* Distinct regulatory properties of pyruvate dehydrogenase kinase and phosphatase isoforms. *Prog Nucleic Acid Res Mol Biol* 2001; **70**: 33–75.
16 Soga T. Cancer metabolism: key players in metabolic reprogramming. *Cancer Sci* 2013; **104**: 275–81.
17 Kaplon J, Zheng L, Meissl K *et al.* A key role for mitochondrial gatekeeper pyruvate dehydrogenase in oncogene-induced senescence. *Nature* 2013; **498**: 109–12.
18 Lyshchik A, Higashi T, Hara T *et al.* Expression of glucose transporter-1, hexokinase-II, proliferating cell nuclear antigen and survival of patients with pancreatic cancer. *Cancer Invest* 2007; **25**: 154–62.

19 Lugli A, Karamitopoulou E, Zlobec I. Tumour budding: a promising parameter in colorectal cancer. *Br J Cancer* 2012; **106**: 1713–7.
20 Ueno H, Hase K, Hashiguchi Y *et al.* Novel risk factors for lymph node metastasis in early invasive colorectal cancer: a multi-institution pathology review. *J Gastroenterol* 2013; Epub ahead of print.
21 Ueno H, Mochizuki H, Hashiguchi Y *et al.* Risk factors for an adverse outcome in early invasive colorectal carcinoma. *Gastroenterology* 2004; **127**: 385–94.
22 Ueno H, Murphy J, Jass JR, Mochizuki H, Talbot IC. Tumour 'budding' as an index to estimate the potential of aggressiveness in rectal cancer. *Histopathology* 2002; **40**: 127–32.
23 Brenner H, Kloor M, Pox CP. Colorectal cancer. *Lancet* 2014; **383**: 1490–502.
24 Hanahan D, Weinberg RA. Hallmarks of cancer: the next generation. *Cell* 2011; **144**: 646–74.
25 Rees JR, Onwuegbusi BA, Save VE, Alderson D, Fitzgerald RC. *In vivo* and in vitro evidence for transforming growth factor-beta1-mediated epithelial to mesenchymal transition in esophageal adenocarcinoma. *Cancer Res* 2006; **66**: 9583–90.
26 Yokobori T, Iinuma H, Shimamura T *et al.* Plastin3 is a novel marker for circulating tumor cells undergoing the epithelial-mesenchymal transition and is associated with colorectal cancer prognosis. *Cancer Res* 2013; **73**: 2059–69.
27 Okada H, Danoff TM, Kalluri R, Neilson EG. Early role of Fsp1 in epithelial-mesenchymal transformation. *Am J Physiol* 1997; **273**: F563–74.
28 Strutz F, Zeisberg M, Ziyadeh FN *et al.* Role of basic fibroblast growth factor-2 in epithelial-mesenchymal transformation. *Kidney Int* 2002; **61**: 1714–28.
29 Vander Heiden MG, Cantley LC, Thompson CB. Understanding the Warburg effect: the metabolic requirements of cell proliferation. *Science* 2009; **324**: 1029–33.
30 Singleterry J, Sreedhar A, Zhao Y. Components of cancer metabolism and therapeutic interventions. *Mitochondrion* 2014; **6**: 50–55.
31 Talmadge JE, Fidler IJ. AACR centennial series: the biology of cancer metastasis: historical perspective. *Cancer Res* 2010; **70**: 5649–69.
32 Fidler IJ. The pathogenesis of cancer metastasis: the 'seed and soil' hypothesis revisited. *Nat Rev Cancer* 2003; **3**: 453–8.
33 Yachida S, Jones S, Bozic I *et al.* Distant metastasis occurs late during the genetic evolution of pancreatic cancer. *Nature* 2010; **467**: 1114–7.
34 Oshiro R, Yamamoto H, Takahashi H *et al.* C4.4A is associated with tumor budding and epithelial-mesenchymal transition of colorectal cancer. *Cancer Sci* 2012; **103**: 1155–64.
35 Koelzer VH, Karamitopoulou E, Dawson H, Kondi-Pafiti A, Zlobec I, Lugli A. Geographic analysis of RKIP expression and its clinical relevance in colorectal cancer. *Br J Cancer* 2013; **108**: 2088–96.
36 LA Zlobec I. Epithelial mesenchymal transition and tumor budding in aggressive colorectal cancer: tumor budding as oncotarget. *Oncotarget* 2010; **1**: 651–61.
37 Schmoll HJ, Van Cutsem E, Stein A *et al.* ESMO Consensus Guidelines for management of patients with colon and rectal cancer. a personalized approach to clinical decision making. *Ann Oncol* 2012; **23**: 2479–516.
38 Watanabe T, Itabashi M, Shimada Y *et al.* Japanese Society for Cancer of the Colon and Rectum (JSCCR) guidelines 2010 for the treatment of colorectal cancer. *Int J Clin Oncol* 2012; **17**: 1–29.
39 Galamb O, Spisak S, Sipos F *et al.* Reversal of gene expression changes in the colorectal normal-adenoma pathway by NS398 selective COX2 inhibitor. *Br J Cancer* 2010; **102**: 765–73.
40 Lin G, He X, Ji H, Shi L, Davis RW, Zhong S. Reproducibility probability score–incorporating measurement variability across laboratories for gene selection. *Nat Biotechnol* 2006; **24**: 1476–7.
41 Skrzypczak M, Goryca K, Rubel T *et al.* Modeling oncogenic signaling in colon tumors by multidirectional analyses of microarray data directed for maximization of analytical reliability. *PLoS ONE* 2010; **5**: e13091.
42 Smith JJ, Deane NG, Wu F *et al.* Experimentally derived metastasis gene expression profile predicts recurrence and death in patients with colon cancer. *Gastroenterology* 2010; **138**: 958–68.
43 Staub E, Groene J, Heinze M *et al.* An expression module of WIPF1-coexpressed genes identifies patients with favorable prognosis in three tumor types. *J Mol Med* 2009; **87**: 633–44.
44 Feron O. Pyruvate into lactate and back: from the Warburg effect to symbiotic energy fuel exchange in cancer cells. *Radiother Oncol* 2009; **92**: 329–33.
45 Semenza GL. Tumor metabolism: cancer cells give and take lactate. *J Clin Invest* 2008; **118**: 3835–7.
46 Kennedy KM, Dewhirst MW. Tumor metabolism of lactate: the influence and therapeutic potential for MCT and CD147 regulation. *Future Oncol* 2010; **6**: 127–48.
47 Hurd TR, DeGennaro M, Lehmann R. Redox regulation of cell migration and adhesion. *Trends Cell Biol* 2012; **22**: 107–15.

Supporting Information

Additional supporting information may be found in the online version of this article:

Fig. S1. Western blot analysis of extracts from HEK293, HeLa cells and three clinical samples of colorectal cancer using Hexokinase 2 antibody.

Fig. S2. Western blot analysis of extracts from HEK293 cell and three clinical samples of colorectal cancer using p-PDH antibody.

Fig. S3. Western blot analysis of extracts from HEK293 cell and three clinical samples of colorectal cancer using PDH-E1α antibody.

Fig. S4. Absorption test of HK2 antibody on pancreatic cancer (A) and colorectal cancer tissues (B–D). Scale bar, 100 μm.

Role of pyruvate kinase M2 in transcriptional regulation leading to epithelial–mesenchymal transition

Atsushi Hamabe[a,b,1], Masamitsu Konno[b,1], Nobuhiro Tanuma[c], Hiroshi Shima[c], Kenta Tsunekuni[a,d,e], Koichi Kawamoto[a,b], Naohiro Nishida[b], Jun Koseki[e], Koshi Mimori[f], Noriko Gotoh[g], Hirofumi Yamamoto[a], Yuichiro Doki[a,b,e], Masaki Mori[a,b,e,2], and Hideshi Ishii[b,e,2]

Departments of [a]Gastrointestinal Surgery and [b]Frontier Science for Cancer and Chemotherapy, Graduate School of Medicine, Osaka University, Osaka 565-0871, Japan; [c]Division of Cancer Chemotherapy, Miyagi Cancer Center Research Institute, Sendai 981-1293, Japan; [d]Taiho Pharmaceutical Co., Ltd., Chiyoda-ku, Tokyo 101-0054, Japan; [e]Department of Cancer Profiling Discovery, Graduate School of Medicine, Osaka University, Osaka 565-0871, Japan; [f]Department of Surgery, Kyushu University Beppu Hospital, Beppu 874-0838, Japan; and [g]Division of Cancer Cell Biology, Cancer Research Institute of Kanazawa University, Kanazawa 920-1192, Japan

Edited by Carlo M. Croce, The Ohio State University, Columbus, OH, and approved September 25, 2014 (received for review May 2, 2014)

Pyruvate kinase M2 (PKM2) is an alternatively spliced variant of the pyruvate kinase gene that is preferentially expressed during embryonic development and in cancer cells. PKM2 alters the final rate-limiting step of glycolysis, resulting in the cancer-specific Warburg effect (also referred to as aerobic glycolysis). Although previous reports suggest that PKM2 functions in nonmetabolic transcriptional regulation, its significance in cancer biology remains elusive. Here we report that stimulation of epithelial–mesenchymal transition (EMT) results in the nuclear translocation of PKM2 in colon cancer cells, which is pivotal in promoting EMT. Immunoprecipitation and LC-electrospray ionized TOF MS analyses revealed that EMT stimulation causes direct interaction of PKM2 in the nucleus with TGF-β–induced factor homeobox 2 (TGIF2), a transcriptional cofactor repressor of TGF-β signaling. The binding of PKM2 with TGIF2 recruits histone deacetylase 3 to the E-cadherin promoter sequence, with subsequent deacetylation of histone H3 and suppression of E-cadherin transcription. This previously unidentified finding of the molecular interaction of PKM2 in the nucleus sheds light on the significance of PKM2 expression in cancer cells.

pyruvate kinase M2 | epithelial–mesenchymal transition | colorectal cancer | invasion | transforming growth factor-β–induced factor homeobox 2

Colorectal cancer (CRC) is the second most common cancer in the world, with more than 1.2 million new cases and about 600,000 deaths annually (1). Cancerous cells exploit a cancer-specific glycolytic system known as the Warburg effect (also referred to as aerobic glycolysis), which involves rapid glucose uptake and preferential conversion to lactate, despite an abundance of oxygen (2, 3). The precise mechanism underpinning aerobic glycolysis was unclear for a long time. However, in 2008, pyruvate kinase M2 (PKM2) gained attention when its expression was shown to be required for the maintenance of aerobic glycolysis (4). PKM2 is an alternatively spliced variant of the PKM gene that regulates the final rate-limiting step of glycolysis. PKM2 is expressed during embryonic development, but it is generally not expressed in most adult tissues. However, its counterpart, PKM1, is exclusively expressed in adult tissues. PKM2 has been shown to be reactivated in tumor development (5, 6). In cancer cells, PKM2 expression allows the diversion of glycolytic flux into the pentose phosphate pathway associated with attenuated pyruvate kinase activity, thereby meeting the biosynthetic demands for rapid proliferation (3).

Investigations about the nuclear function of PKM2 arose after elucidation of the PKM2 metabolic function. It was identified that in cancer cells, PKM2 can translocate into the nucleus and function as a transcriptional cofactor in response to several extracellular signals, including EGF and hypoxia, subsequently activating CYCLIN D1, C-MYC, or hypoxia-inducible factor 1α (HIF-1α) (7, 8). Particularly in the hypoxic condition, PKM2 interacts with HIF-1α and participates in a positive feedback loop, thereby enhancing HIF-1α transactivation and reprogramming glucose metabolism by regulating the expression of glycolysis-associated enzymes (8). This finding suggested that the PKM2 nuclear function may operate upstream of metabolic regulation and that the resultant metabolic reprogramming and oncogene activation by PKM2 work cooperatively to promote cancer cell proliferation and tumor growth.

In addition to proliferation maintenance and growth suppression prevention, invasion and metastasis have also been targeted as hallmarks of cancer (9). In the invasion process, cancer cells acquire the ability to dissociate from the bulk of the tumor and to migrate into the surrounding stroma, which is regulated by epithelial–mesenchymal transition (EMT) (9, 10). During EMT, cancer cells lose their cell-to-cell contacts by

Significance

Our study shows that pyruvate kinase M2 (PKM2), an alternatively spliced variant of the pyruvate kinase gene, mediates epithelial–mesenchymal transition (EMT), which is critical for cancer cells to acquire invasive potential. Our study demonstrates that EMT stimulates nuclear translocation of PKM2 and decreases epithelial cadherin transcription (a requirement for EMT induction). Our results also demonstrate that PKM2 interacts with the transcriptional factor TGF-β–induced factor homeobox 2, which induces the deacetylation of histone H3, resulting in repressed E-cadherin expression. The precise understanding of nuclear PKM2 function suggests the potential for a model preventing cancer metastasis.

Author contributions: A.H., M.K., K.T., K.K., N.N., J.K., K.M., N.G., H.Y., Y.D., M.M., and H.I. designed research; A.H., M.K., and H.I. performed research; A.H., M.K., N.T., H.S., and H.I. contributed new reagents/analytic tools; A.H., M.K., J.K., N.G., M.M., and H.I. analyzed data; and A.H., M.K., N.T., H.S., K.T., K.K., N.N., J.K., K.M., N.G., M.M., and H.I. wrote the paper.

Conflict of interest statement: This work was supported in part by a Grant-in-Aid for Scientific Research from the Ministry of Education, Culture, Sports, Science, and Technology; a Grant-in-Aid from the Third Comprehensive 10-year Strategy for Cancer Control, Ministry of Health, Labor, and Welfare; a grant from the Kobayashi Cancer Research Foundation; a grant from the Princess Takamatsu Cancer Research Fund, Japan; a grant from the National Institute of Biomedical Innovation; and a grant from the Osaka University Drug Discovery Funds. A.H. is a research fellow of the Japan Society for the Promotion of Science. Partial support was received from Taiho Pharmaceutical Co., Ltd. (to J.K., M.M., and H.I.), Chugai Co., Ltd., Yakult Honsha Co., Ltd., Merck Co., Ltd., Takeda Science Foundation, and Takeda Medical Research Foundation (to M.K., N.N., M.M., and H.I.) through institutional endowments.

This article is a PNAS Direct Submission.

[1]A.H. and M.K. contributed equally to this work.

[2]To whom correspondence may be addressed. Email: mmori@gesurg.med.osaka-u.ac.jp or hishii@gesurg.med.osaka-u.ac.jp.

This article contains supporting information online at www.pnas.org/lookup/suppl/doi:10.1073/pnas.1407717111/-/DCSupplemental.

inhibiting epithelial cadherin (E-cadherin; encoded by *CDH1*) expression and acquiring mesenchymal markers. This process is physiologically important during embryogenesis and is required for in utero development. Given that PKM2 expression and EMT are common to both tumorigenesis and development, PKM2 may affect EMT within cancer cells. However, the significance of PKM2 during EMT or invasion is yet to be investigated.

In the present study, we demonstrate that PKM2 translocates into the nucleus during EMT and acts as a transcription cofactor that inhibits *CDH1* expression. PKM2 interacts with TGF-β–induced factor homeobox 2 (TGIF2), which recruits histone deacetylase 3 (HDAC3) to the promoter sequence of E-cadherin, thereby promoting histone H3 lysine 9 (H3K9) deacetylation and *CDH1* expression down-regulation.

Results

EMT Induction Elicits Nuclear Translocation of PKM2. For the induction of EMT, we cultured colon cancer cells in a medium with TGF-β1 and EGF, as described previously (Fig. 1*A*) (11–14). The SW480 cells changed morphology from epithelial to fibroblastic-like and spindle-shaped in a time-dependent manner (Fig. 1*B*). Consistent with this observation, *CDH1* transcript expression was suppressed, whereas the expression levels of the vimentin (*VIM*), zinc finger e-box binding homeobox 1 (*ZEB1*), and snail family zinc finger 2 (*SNAI2*) genes were increased (Fig. 1*C*). PK gene expression was induced in the EMT condition, with preferential expression of PKM2 compared with PKM1 (Fig. 1*D*). Western blot analysis indicated that the induction of EMT resulted in decreased *CDH1* expression, increased *VIM* expression, and up-regulated PKM2 (Fig. 1*E*). We confirmed that the expression and secretion of endogenous TGF-β1 was minimal in SW480 (Fig. S1 *A* and *B*).

To determine the intracellular localization of proteins, cytoplasmic and nuclear fractions were separated from the EMT-induced cells and Western blot analysis was performed. The data indicated that, although the EMT condition stimulated an increase in cytoplasmic PKM2, nuclear PKM2 was augmented compared with levels in the pre-EMT state (Fig. 1*F*). Immunocytochemistry and immunofluorescence intensity quantification confirmed the increase in nuclear PKM2 (Fig. S2 *A–D*). In addition, we confirmed that nuclear PKM2 was also increased in HCT116 cells under the same EMT condition (Fig. S2*E*) and that the expression of EMT markers was increased in murine *Pkm2* knock-in, compared with *Pkm1* knock-in, mesencymal cells, as well as other human cancer cells (Fig. S1 *C* and *D*).

Previous studies showed that EGF stimulation increased nuclear PKM2 (7) and indicated that cytoplasmic PKM2 functions with tetramer formation, whereas nuclear PKM2 functions with dimer formation. Given that the large hydrophobic hole at the nucleotide binding site is buried in tetrameric PKM2 structure, which becomes accessible in dimer form (15), the dimer formation may provide a protein binding ability. We studied the status of PKM2 during EMT and found that simultaneous stimulation by TGF-β1 and EGF, in comparison with either alone, resulted in increased expression of an ~120-kDa complex, corresponding to dimeric PKM2 (Fig. 1*G* and Fig. S3). The present study demonstrated that PKM2 nuclear translocation was stimulated in the EMT condition, suggesting a unique function of PKM2 in the nucleus.

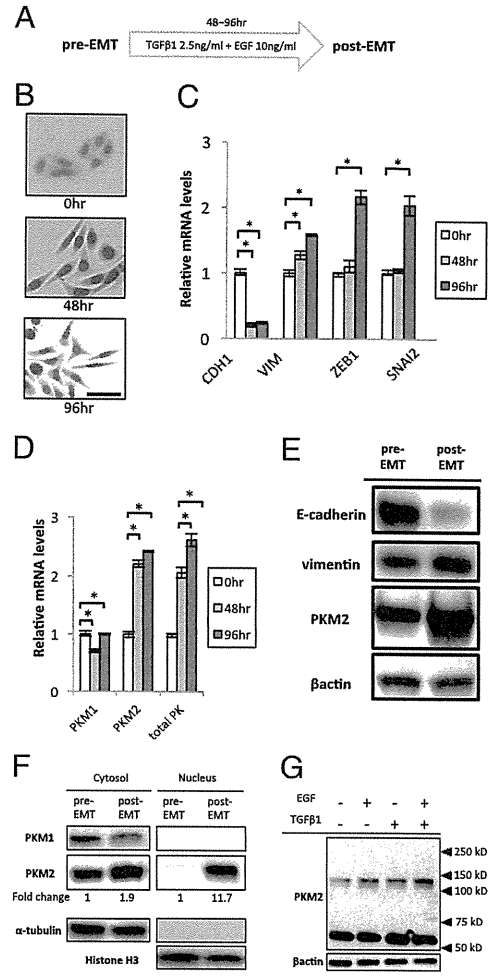

Fig. 1. PKM2 translocates into the nucleus during EMT. (*A*) Schematic representation of the procedure for EMT induction. The cells incubated for 48 h after seeding are defined as pre-EMT, and the cells cultured with 2.5 ng/mL TGF-β1 and 10 ng/mL EGF are defined as post-EMT. (*B*) Photomicrographs of the morphological change in SW480 cells. The cells were stained using the Diff-Quik Kit (Sysmex Corp.). The number of hours indicates the period since EMT induction was initiated. (Scale bar, 100 μm.) (*C*) Relative transcript (mRNA) levels of *CDH1*, *VIM*, *ZEB1*, and *SNAI2* after induction of EMT for 0, 48, and 96 h. The values at 0 h (pre-EMT) have been normalized to 1, and the data are expressed as fold. (*D*) Relative mRNA levels of PKM1, PKM2, and pyruvate kinase (total PK) after induction of EMT for 0, 48, and 96 h. (*E*) Western blot assays of E-cadherin, vimentin, and PKM2 expression in pre-EMT and post-EMT cells. Post-EMT cells were harvested at 72 h. (*F*) Western blot assays of PKM1, PKM2, α-tubulin, and histone H3 in nuclear and cytoplasmic lysates prepared from SW480 cells. With normalization to cytoplasmic tubulin or nuclear histone H3 blots, the relative intensities of PKM2 blots are shown in comparison with those in the pre-EMT condition. (*G*) SW480 cells were treated with dimethyl suberimidate for 30–60 min, immediately followed by whole cell lysis. The monomer and dimer states of PKM2 were analyzed by Western blot assay. Columns represent the average of at least three independent experiments; error bars represent the SD of the mean from triplicate results. $*P < 0.05$.

PKM2 Expression Is Required to Induce EMT. To investigate the causative role of PKM2 in EMT induction, we cultured cells with endogenous PKM2 inhibition by small interfering RNA (siRNA) knockdown (KD) under EMT conditions. We used the siRNA targeting system, which reportedly inhibits PKM2 without any off-target effects on other genes (16), and the results indicate that the most effective siRNA sequence could inhibit transcriptional and translational levels of PKM2, whereas those of PKM1 were increased (Fig. S4 *A* and *B*). PKM2 KD failed to induce spindle-shaped morphological changes under EMT conditions (Fig. 2*A*). Expression analysis indicated that PKM2 KD prevented *CDH1* down-regulation, although *VIM* expression persisted (Fig. 2*B*), suggesting a role for PKM2 in *CDH1* transcription. Fifty percent reductions in glucose or glutamine in the medium did not have significant effects on EMT marker expression (Fig. S5*A*), suggesting distinct effects on EMT and metabolism.

Western blot analysis indicated that PKM2 KD hindered *CDH1* loss and *VIM* gain compared with the control (Fig. 2*C*).

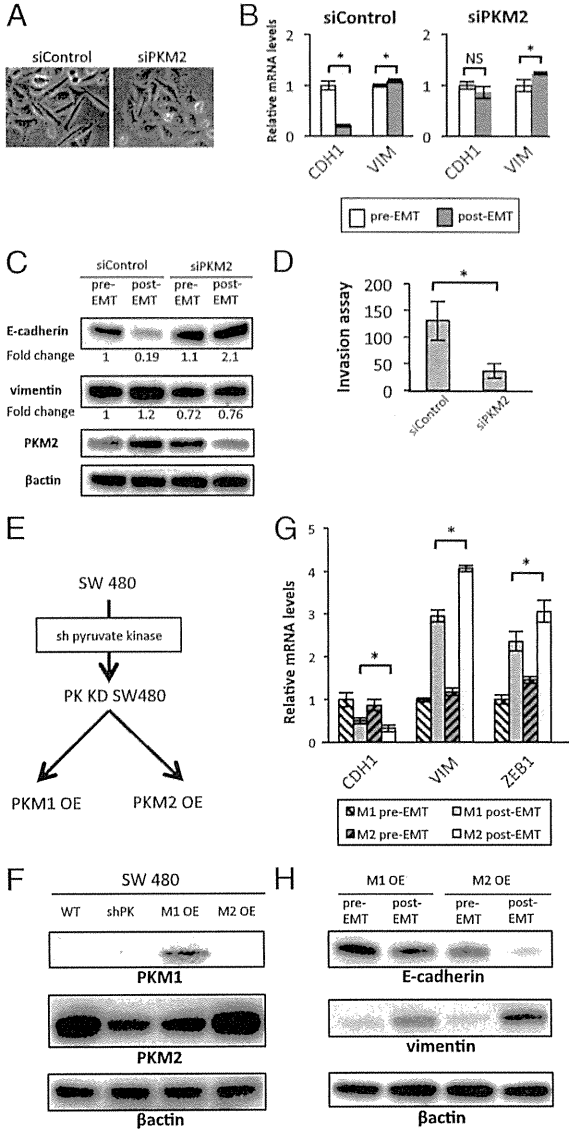

Fig. 2. PKM2 is required for EMT induction. (*A*) Phase-contrast photomicrographs of SW480 cells transfected with siControl or siPKM2 after EMT induction for 48 h. (*B*) Relative transcript (mRNA) levels of *CDH1* and *VIM* after EMT induction in cells transfected with siControl or siPKM2 for 48 h. (*C*) Western blot assays of E-cadherin, vimentin, PKM2, and β-actin expression in pre-EMT and post-EMT cells. Post-EMT cell samples were harvested at 72 h. With normalization to β-actin as a control, the relative intensities of E-cadherin and vimentin are shown in comparison with those in the control pre-EMT condition. Note that siPKM2 knockdown works efficiently in post-EMT cells. (*D*) Invasive behavior of SW480 cells treated with siControl or siPKM2. (*E*) Schematic procedure for establishing PKM1 OE or PKM2 OE SW480 cells. (*F*) Western blot assays of PKM1, PKM2, and β-actin expression in WT SW480 cells, cells stably expressing shRNA constructs targeting pyruvate kinase (shPK), and shPK cells overexpressing either PKM1 or PKM2 constructs. (*G*) Relative mRNA levels of *CDH1*, *VIM*, and *ZEB1* after EMT induction in PKM1 OE or PKM2 OE SW480 cells for 72 h. (*H*) Western blot assays of E-cadherin, vimentin, and β-actin expression in PKM1 OE and PKM2 OE cells. Post-EMT cell samples were harvested at 72 h. Column values = average of at least three independent experiments; error bars represent SD from the mean of triplicate experiments. $*P < 0.05$.

Inhibition of EMT by PKM2 KD resulted in a significant reduction in in vitro cellular invasiveness (Fig. 2*D*). The assessment of mothers against decapentaplegic homolog 2 (SMAD2) and ERK, which are downstream effectors of TGF-β1 and EGF signaling, indicated that PKM2 KD disturbed the phosphorylation process (Fig. S5*B*).

To minimize the effect of an alternative exon and to focus on the function of PKM2 in the nucleus, we established PKM1- and PKM2-overexpressing (OE) cell lines (PKM1 and PKM2 OE in Fig. 2*E*). In brief, we transfected the cells with a small hairpin RNA (shRNA) vector targeting the common region in *PK* and then introduced an overexpression vector of PKM1 or PKM2 cDNA without a complementary sequence to the shRNA (Fig. 2*F*). We cultured the established cells in EMT-inducing conditions. The results demonstrated a greater decrease in *CDH1* expression and greater increase in *VIM* and *ZEB1* expression in PKM2 OE cells compared with that in PKM1 OE cells (Fig. 2*G* and Fig. S4*C*). Consistent results were obtained by Western blot analysis (Fig. 2*H*). These results indicate that PKM2 expression is necessary for EMT induction.

Nuclear PKM2 Binds to TGIF2 and Represses CHD1 Expression. Nuclear PKM2 reportedly binds to and phosphorylates STAT3 through its function as a protein kinase (15). The observation that nuclear PKM2 increased during EMT led us to consider the possibility that PKM2 may interact with other transcription factors. To validate this hypothesis, fractions pulled-down with the PKM2 antibody were subjected to LC-electrospray ionized TOF MS analyses. The result showed that nuclear PKM2 was coimmunoprecipitated with TGIF2 and that this binding was detectable when both EGF and TGFβ1 were added to the culture (Fig. 3*A*). These findings were confirmed by immunoprecipitation, followed by Western blot analysis (Fig. 3*B*). The EMT stimulation resulted in the significant increase of TGIF2 expression (Fig. S6*A*). TGIF2 KD did not show significant alterations of PKM2 expression regardless of EMT induction (Fig. 3*E* and Fig. S6*B*). We could not detect an association of PKM1 with TGIF2 in the nucleus (Fig. S7*A*), which further supports the cytoplasmic localization of PKM1 (Fig. 1*F*).

Melhuish et al. (17) revealed that TGIF2 is a transcriptional repressor that suppresses TGF-β–responsive gene expression by binding to TGF-β–activated SMADs. First, we performed TGIF2 KD, followed by EMT induction (Fig. 3*C* and Fig. S6*B*). TGIF2 KD enhanced the decrease in both the transcriptional and the translational levels of *CDH1* expression (Fig. 3 *D* and *E*). To analyze the difference in the effect of TGIF2 KD in cells expressing either PKM1 or PKM2, we performed TGIF2 KD on PKM1 OE and PKM2 OE cells, followed by EMT induction. Interestingly, the decrease in *CDH1* expression and increase in *VIM* expression were similar at the transcriptional and translational levels after EMT induction in both cell lines (Fig. 3 *F* and *G*). These results indicate that the augmented sensitivity to EMT induction in PKM2 OE cells is abrogated under TGIF2 suppression. These data further suggest that nuclear PKM2 responds to EMT stimulation and interacts with TGIF2 to mediate EMT induction downstream of PKM2.

PKM2 and TGIF2 Recruit HDAC3 to the *CDH1* Promoter to Repress Transcription. TGIF2 is a transcriptional factor that regulates TGF-β signal transduction (17). Based on the above findings, we hypothesized that TGIF2 could bind to the *CDH1* promoter and activate *CDH1* expression in the epithelial state. To examine this hypothesis, we performed a ChIP quantitative PCR (qPCR) assay using two sets of primers located in the *CDH1* promoter sequence region (Fig. 4*A*). We found depressed binding of TGIF2 to the *CDH1* promoter region during EMT (Fig. 4*B*).

TGIF2 can control transcription by recruiting HDAC in response to TGF-β signaling (17) and PKM2 can associate with HDAC3 in the nucleus (7). To investigate whether TGIF2 can bind to HDAC3 during EMT, we performed immunoprecipitation followed by Western blot analysis and found an association between TGIF2 and HDAC3 under EMT induction (Fig. 4*C* and

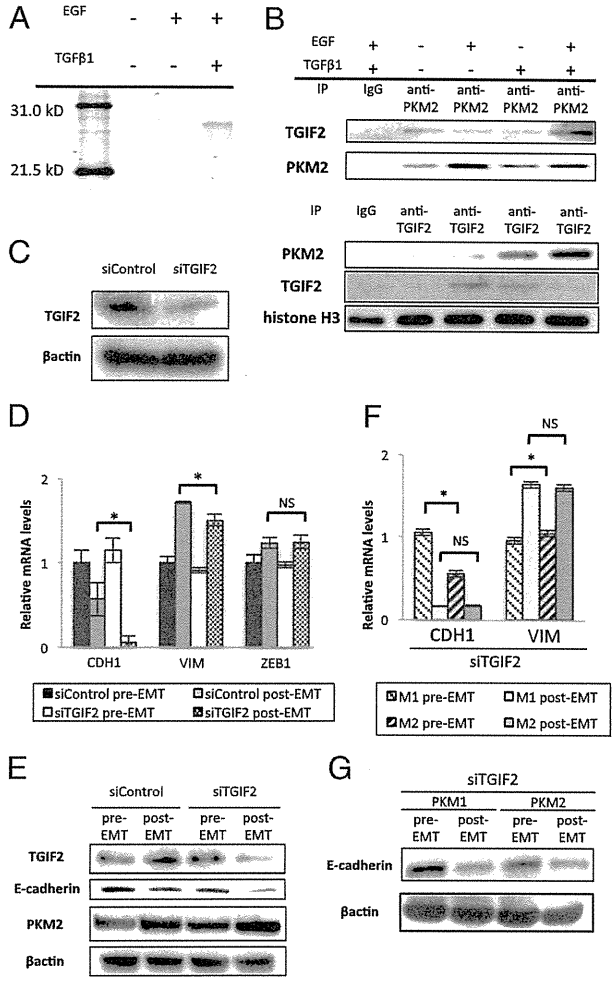

Fig. 3. Interaction between nuclear PKM2 and TGIF2 mediates EMT induction. (*A*) Polyacrylamide gel electrophoresis of proteins immunoprecipitated with anti-PKM2 antibody in the nucleic lysate of cells cultured under normal conditions, with EGF alone, or with TGF-β1 and EGF. The band detected in samples of cells stimulated with TGF-β1 and EGF was excised and analyzed by MS. (*B*) Western blot assays of immunoprecipitated samples of nucleic lysates with anti-PKM2 or anti-TGIF2 antibody. Samples were harvested after the cells were treated as indicated for 72 h. (*C*) Western blot assays of TGIF2 and β-actin expression in cells transfected with siControl or siTGIF2. (*D*) Relative transcript (mRNA) levels of *CDH1*, *VIM*, and *ZEB1* after induction of EMT in cells transfected with siControl or siTGIF2 for 72 h. (*E*) Western blot analysis of TGIF2, E-cadherin, PKM2, and β-actin expression in pre-EMT and post-EMT cells transfected with siControl or siTGIF2. Post-EMT samples were harvested at 72 h, when siRNA inhibition was profound. (*F*) Relative mRNA levels of *CDH1* and *VIM* after EMT induction in PKM1 OE and PKM2 OE cells. Post-EMT samples were harvested at 72 h. (*G*) Western blot analysis of E-cadherin and β-actin after EMT induction in PKM1 OE and PKM2 OE cells transfected with siTGIF2. Post-EMT samples were harvested at 72 h. Column values = average of at least three independent experiments; error bars represent SD from the mean of triplicate experiments. $*P < 0.05$.

Figs. S7*B* and S8). To examine the acetylation status of histone H3 in the *CDH1* promoter region, we performed ChIP qPCR and found that binding of acetylated H3K9 to the *CDH1* promoter was decreased under EMT conditions (Fig. 4*D*). Furthermore, to understand how the PKM2–TGIF2–HDAC3 complex can bind to the *CDH1* promoter, additional ChIP qPCR analysis was performed. The data indicated that similar to the binding of TGIF2, the binding of PKM2 and HDAC3 to the *CDH1* promoter was reduced during EMT (Fig. S9 *A* and *B*). Given that the TGIF2 protein bound to PKM2 and HDAC3 during EMT (Figs. 3*B* and 4*C* and Fig. S7*B*), the present study demonstrates that nuclear PKM2 plays a role in the TGIF2-dependent control of CHD1 expression and that EGF induces formation of the PKM2–TGIF2–HDAC3 complex, followed by histone deacetylation, thus resulting in suppressed *CDH1* expression. TGF-β1 may modulate the association of this complex, although H3K9 was deacetylated (Fig. 5*D*).

PKM2 Expression in the Deepest Tumor Regions Correlated with CRC Metastasis. To investigate the clinical significance of PKM2 expression in cancer metastasis, we immunohistochemically analyzed clinical CRC samples. Staining was assessed in the deepest tumor regions where the CRC invasion begins (18, 19). The

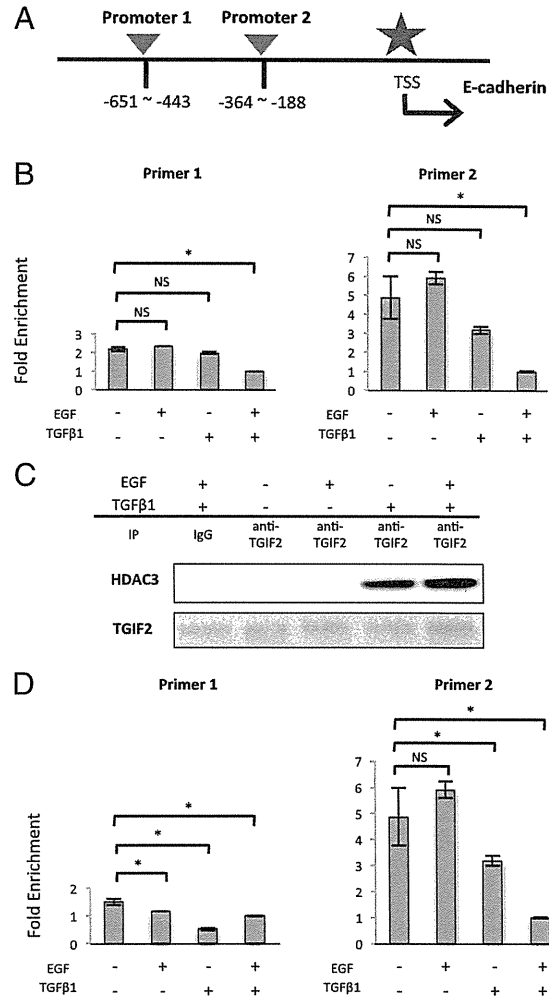

Fig. 4. TGIF2 binds to the CDH promoter and recruits HDAC3 during EMT. (*A*) Schematic diagram showing the positions of two sets of primers designed to cover the promoter region of the *CDH1* gene. (*B*) ChIP assays were performed with IgG and anti-TGIF2 antibody, followed by qPCR (mean ± SD, $n = 3$). ChIP samples were harvested from the nucleic lysate of SW480 cells treated as indicated for 72 h. (*C*) Western blot assays of immunoprecipitated samples of nucleic lysate with anti-TGIF2 antibody. Each sample was harvested after the cells were treated as indicated for 72 h. (*D*) ChIP assays were performed with IgG and anti-acetylated H3K9 antibody, followed by qPCR (mean ± SD, $n = 3$). ChIP samples were harvested from the nucleic lysate of SW480 cells treated as indicated for 72 h. Column values = average of at least three independent experiments; error bars represent SD from the mean of triplicate experiments. $*P < 0.05$.

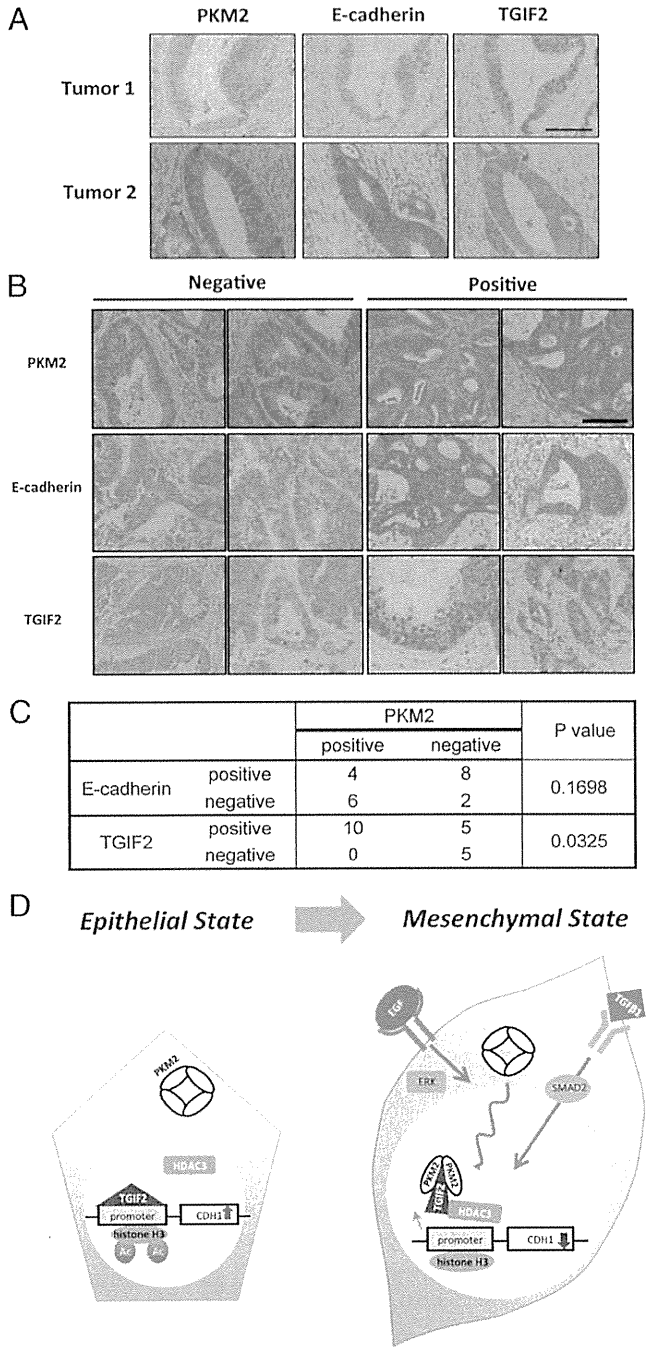

		PKM2 positive	PKM2 negative	P value
E-cadherin	positive	4	8	0.1698
	negative	6	2	
TGIF2	positive	10	5	0.0325
	negative	0	5	

Fig. 5. The immunohistochemistry. (*A*) Staining at the invasive front, showing an inverse correlation between PKM2, E-cadherin, and TGIF2 expression. (Scale bar, 100 μm.) (*B*) The representative cases are shown for staining for PKM2, TGIF2, and E-cadherin. Invasive fronts of tumors were stained by anti-PKM2, anti-E-cadherin, and anti-TGIF2 antibodies, and the intensities were assigned to positive and negative groups. With regard to TGIF2 staining, under the microscopic observation, cases with more than 50% of cells stained in nucleus were designated as positive, whereas the others were negative. (*C*) The 10 positive and 10 negative cases for cellular PKM2 were examined for nuclear TGIF2 and membranous E-cadherin. (*D*) Theoretical model illustrating the functional roles of PKM2 and TGIF2 in regulating *CDH1* transcription during EMT.

PKM2 staining intensities were assigned to positive and negative groups (Fig. 5 *A*–*C*). The correlations between PKM2 expression and clinicopathological factors are summarized in Table S1. PKM2-positive staining was significantly correlated with metastasis to lymph nodes and distant organs. To further understand the clinical significance of PKM2 in CRC, we analyzed the GSE17536 database of the gene expression array and patient prognosis. To study the specific effect of PKM2 in the array database, we analyzed expression of both PK and its splicing factor hnRNPA2, because hnRNPA2 stimulates the splicing to PKM2 (20, 21). As expected, cases with high PK and high hnRNPA2 expression showed a poorer prognosis than other groups; the difference in prognosis was apparent in stages III and IV with metastasis (Fig. S10 *A* and *B*). The data confirmed that PKM2 can enhance the ability of cancer cells to metastasize in primary cancer tissues.

Discussion

In the present study, we demonstrated that nuclear PKM2 interacts with TGIF2 during EMT, which is pivotal in promoting the transition into the mesenchymal cancer cell phenotype. Consequently, we propose a model for the nuclear PKM2 function in response to EMT stimulation (Fig. 5*D*). Under epithelial conditions, histone H3 is acetylated on the *CDH1* promoter region and *CDH1* is transcribed where TGIF2 should serve as an active transcription factor. Once the EMT signal stimulates transformation of the cancer cell, a PKM2 fraction enters the nucleus and associates with TGIF2. We assume that this association will alter the conformation of TGIF2 or its associated complexes, effectively loosening the binding between TGIF2 and the *CDH1* promoter sequence to allow the recruitment of HDAC3 and subsequent histone H3 deacetylation. *CDH1* expression is suppressed as a consequence of the downregulated promoter activity. In this context, nuclear PKM2 serves as a transcriptional cofactor regulating TGIF2 behavior.

Few reports have investigated the significance of TGIF2 in cancer. In ovarian cancer, TGIF2 is reportedly amplified and overexpressed (22), whereas a comparison between colorectal adenoma and colorectal carcinoma revealed that TGIF2 expression is increased only in the latter (23). Further, TGIF2 has been shown to interact with TGF-β–activated SMADs and be able to repress the activation of TGF-β–responsive transcription (17). The present study demonstrated that TGIF2 affects *CDH1* expression through the regulation of promoter activity in which TGIF2 is supposed to function as an activating transcription factor.

TGF-β1 is a multifunctional cytokine that has dual and opposing roles in controlling cell fate. In the early stages of cancer, TGF-β1 induces growth arrest and apoptosis, exerting tumor-suppressive effects, whereas in later stages, TGF-β1 enhances tumor progression by provoking a variety of malignancy-related responses, including EMT (24–26). This paradox remains unsolved despite numerous studies addressing the issue. However, based on the results in the present study, we propose that the interaction between PKM2 and TGIF2 may offer a plausible explanation. In normal cells, PK expression is exclusively shifted to PKM1, but on TGF-β signaling, TGIF2 can suppress transcription downstream of the SMAD signal. Conversely, in cancer cells abundantly expressing PKM2, PKM2 translocates and is bound to TGIF2 in the nucleus, thereby reversing TGF-β signal transduction. Further investigation is necessary to determine the significance of TGIF2 expression and the precise mechanism underlying this interaction.

Nuclear PKM2 forms a dimer and functions as a protein kinase, whereas cytoplasmic PKM2 forms a tetramer and functions as a pyruvate kinase (15). In the present study, the dimeric form of PKM2 was increased, suggesting that the protein kinase activity of PKM2 is enhanced during EMT. PKM2 translocates into the nucleus in response to variable signals, of which, the EGF–ERK pathway is the most investigated (7, 27). Interestingly, TGIF2 is phosphorylated in response to EGF signaling (17). Given that EGF induces nuclear translocation of PKM2, PKM2 may function as a dimeric protein kinase in the

nucleus, phosphorylating TGIF2. However, the phosphorylation status of TGIF2 was not addressed in our study. Gao et al. (15) demonstrated that PKM2 interacts with STAT3 to control downstream gene expression in SW480 cells. Thus, it is conceivable that the molecular interaction of PKM2 is highly context dependent, with cell fate determined by how nuclear PKM2 regulates gene expression.

PKM2 has both metabolic and nonmetabolic functions, which are essential in the cytoplasm and nucleus, respectively. Increasing evidence has suggested that nuclear PKM2 binds to numerous transcriptional factors, thereby conferring cells with advanced malignant potential. The present study determined that PKM2 significantly influences EMT induction by modulating *CDH1* expression, thus providing a molecular basis for EMT acquisition. Future cancer treatments may be able to target the inhibition of nuclear PKM2.

Methods

Cell Lines and Culture. The human colorectal cancer cell lines, SW480 and HCT116, were obtained from ATCC, and CaR-1 was obtained from JCRB. These cell lines were grown in DMEM (Sigma-Aldrich) supplemented with 10% (vol/vol) FBS (Thermo Fisher Scientific), 100 U/mL penicillin, and 100 U/mL streptomycin (Life Technologies) and grown at 37 °C in a humidified incubator with 5% CO_2.

EMT Induction. Cells were seeded at a concentration of 5.0×10^4 cells/mL and incubated in a humidified atmosphere (37 °C and 5% CO_2) in standard medium for 48 h, after which they were treated with TGF-β1 (2.5 ng/mL; Sigma-Aldrich). Next, they were incubated with MEM supplemented with 10 ng/mL FBS-free EGF (Sigma-Aldrich), 100× insulin-transferring selenium (ITS; Life Technologies), and 50 nmol/L hydrocortisone (Tokyo Kasei) for 48–96 h.

ACKNOWLEDGMENTS. We thank the members of our laboratories for helpful discussions; Idea Consultants, Inc. (Osaka, Japan) and Olympus Co. (Tokyo, Japan) for technical assistance; Lewis C. Cantley for providing the lentiviral shRNA and retroviral expression vector; and H. Miyoshi for providing the packaging plasmids.

1. Jemal A, et al. (2011) Global cancer statistics. *CA Cancer J Clin* 61(2):69–90.
2. Warburg O (1956) On the origin of cancer cells. *Science* 123(3191):309–314.
3. Vander Heiden MG, Cantley LC, Thompson CB (2009) Understanding the Warburg effect: The metabolic requirements of cell proliferation. *Science* 324(5930):1029–1033.
4. Christofk HR, et al. (2008) The M2 splice isoform of pyruvate kinase is important for cancer metabolism and tumour growth. *Nature* 452(7184):230–233.
5. Hacker HJ, Steinberg P, Bannasch P (1998) Pyruvate kinase isoenzyme shift from L-type to M2-type is a late event in hepatocarcinogenesis induced in rats by a choline-deficient/DL-ethionine-supplemented diet. *Carcinogenesis* 19(1):99–107.
6. Elbers JR, et al. (1991) Pyruvate kinase activity and isozyme composition in normal fibrous tissue and fibroblastic proliferations. *Cancer* 67(10):2552–2559.
7. Yang W, et al. (2011) Nuclear PKM2 regulates β-catenin transactivation upon EGFR activation. *Nature* 480(7375):118–122.
8. Luo W, et al. (2011) Pyruvate kinase M2 is a PHD3-stimulated coactivator for hypoxia-inducible factor 1. *Cell* 145(5):732–744.
9. Hanahan D, Weinberg RA (2011) Hallmarks of cancer: The next generation. *Cell* 144(5):646–674.
10. Weinberg RA (2008) Mechanisms of malignant progression. *Carcinogenesis* 29(6): 1092–1095.
11. Rees JR, Onwuegbusi BA, Save VE, Alderson D, Fitzgerald RC (2006) In vivo and in vitro evidence for transforming growth factor-beta1-mediated epithelial to mesenchymal transition in esophageal adenocarcinoma. *Cancer Res* 66(19):9583–9590.
12. Yokobori T, et al. (2013) Plastin3 is a novel marker for circulating tumor cells undergoing the epithelial-mesenchymal transition and is associated with colorectal cancer prognosis. *Cancer Res* 73(7):2059–2069.
13. Okada H, Danoff TM, Kalluri R, Neilson EG (1997) Early role of Fsp1 in epithelial-mesenchymal transformation. *Am J Physiol* 273(4 Pt 2):F563–F574.
14. Strutz F, et al. (2002) Role of basic fibroblast growth factor-2 in epithelial-mesenchymal transformation. *Kidney Int* 61(5):1714–1728.
15. Gao X, Wang H, Yang JJ, Liu X, Liu ZR (2012) Pyruvate kinase M2 regulates gene transcription by acting as a protein kinase. *Mol Cell* 45(5):598–609.
16. Goldberg MS, Sharp PA (2012) Pyruvate kinase M2-specific siRNA induces apoptosis and tumor regression. *J Exp Med* 209(2):217–224.
17. Melhuish TA, Gallo CM, Wotton D (2001) TGIF2 interacts with histone deacetylase 1 and represses transcription. *J Biol Chem* 276(34):32109–32114.
18. Lugli A, Karamitopoulou E, Zlobec I (2012) Tumour budding: A promising parameter in colorectal cancer. *Br J Cancer* 106(11):1713–1717.
19. Ueno H, et al. (2014) Novel risk factors for lymph node metastasis in early invasive colorectal cancer: A multi-institution pathology review. *J Gastroenterol* 49(9):1314–1323.
20. Clower CV, et al. (2010) The alternative splicing repressors hnRNP A1/A2 and PTB influence pyruvate kinase isoform expression and cell metabolism. *Proc Natl Acad Sci USA* 107(5):1894–1899.
21. David CJ, Chen M, Assanah M, Canoll P, Manley JL (2010) HnRNP proteins controlled by c-Myc deregulate pyruvate kinase mRNA splicing in cancer. *Nature* 463(7279): 364–368.
22. Imoto I, et al. (2000) Amplification and overexpression of TGIF2, a novel homeobox gene of the TALE superclass, in ovarian cancer cell lines. *Biochem Biophys Res Commun* 276(1):264–270.
23. Lips EH, et al. (2008) Integrating chromosomal aberrations and gene expression profiles to dissect rectal tumorigenesis. *BMC Cancer* 8:314.
24. Roberts AB, Wakefield LM (2003) The two faces of transforming growth factor beta in carcinogenesis. *Proc Natl Acad Sci USA* 100(15):8621–8623.
25. Tian M, Schiemann WP (2009) The TGF-beta paradox in human cancer: An update. *Future Oncol* 5(2):259–271.
26. Rahimi RA, Leof EB (2007) TGF-beta signaling: A tale of two responses. *J Cell Biochem* 102(3):593–608.
27. Yang W, et al. (2012) ERK1/2-dependent phosphorylation and nuclear translocation of PKM2 promotes the Warburg effect. *Nat Cell Biol* 14(12):1295–1304.

Biomaterials 39 (2015) 23–30

Contents lists available at ScienceDirect

Biomaterials

journal homepage: www.elsevier.com/locate/biomaterials

Antibody fragment-conjugated polymeric micelles incorporating platinum drugs for targeted therapy of pancreatic cancer

Jooyeon Ahn [a], Yutaka Miura [b], Naoki Yamada [d], Tsukasa Chida [a], Xueying Liu [b], Ahram Kim [a], Ryuta Sato [e], Ryo Tsumura [e], Yoshikatsu Koga [e], Masahiro Yasunaga [e], Nobuhiro Nishiyama [d], Yasuhiro Matsumura [e], Horacio Cabral [a], Kazunori Kataoka [a, b, c, *]

[a] Department of Bioengineering, Graduate School of Engineering, The University of Tokyo, 7-3-1 Hongo, Bunkyo-ku, Tokyo 113-8656, Japan
[b] Division of Clinical Biotechnology, Center for Disease Biology and Integrative Medicine, Graduate School of Medicine, The University of Tokyo, 7-3-1 Hongo, Bunkyo-ku, Tokyo 113-0033, Japan
[c] Department of Materials Engineering, Graduate School of Engineering, The University of Tokyo, 7-3-1 Hongo, Bunkyo-ku, Tokyo 113-8656, Japan
[d] Polymer Chemistry Division, Chemical Resources Laboratory, Tokyo Institute of Technology, R1-11, 4259 Nagatsuta, Midori-ku, Yokohama 226-8503, Japan
[e] Division of Developmental Therapeutics, National Cancer Center Hospital East, 6-5-1 Kashiwanoha, Kashiwa, Chiba 277-8577, Japan

ARTICLE INFO

Article history:
Received 13 August 2014
Accepted 20 October 2014
Available online 15 November 2014

Keywords:
Drug delivery
Platinum
Micelle
Nanoparticle
Chemotherapy

ABSTRACT

Antibody-mediated therapies including antibody-drug conjugates (ADCs) have shown much potential in cancer treatment by tumor-targeted delivery of cytotoxic drugs. However, there is a limitation of payloads that can be delivered by ADCs. Integration of antibodies to drug-loaded nanocarriers broadens the applicability of antibodies to a wide range of therapeutics. Herein, we developed antibody fragment-installed polymeric micelles *via* maleimide-thiol conjugation for selectively delivering platinum drugs to pancreatic tumors. By tailoring the surface density of maleimide on the micelles, one tissue factor (TF)-targeting Fab' was conjugated to each carrier. Fab'-installed platinum-loaded micelles exhibited more than 15-fold increased cellular binding within 1 h and rapid cellular internalization compared to non-targeted micelles, leading to superior *in vitro* cytotoxicity. *In vivo*, Fab'-installed micelles significantly suppressed the growth of pancreatic tumor xenografts for more than 40 days, outperforming non-targeted micelles and free drugs. These results indicate the potential of Fab'-installed polymeric micelles for efficient drug delivery to solid tumors.

1. Introduction

Antibody-drug conjugates (ADCs) are attracting much interest in cancer therapy [1,2] due to the improvement of therapeutic efficacies by selectively delivering anticancer drugs to cancer cells compared to conventional chemotherapies. The development of ADCs has been one of the most active areas in recent years, and as much as thirty ADCs have entered clinical evaluation in 2013 for the treatment of solid tumors and leukemia [3]. Nevertheless, a major challenge in the development of ADCs is the limited amounts of drugs that can be delivered by a single antibody, as overloading may reduce the binding affinity of the antibody or affect the pharmacokinetics [4,5]. Thus, 2 to 4 cytotoxins per antibody are generally introduced in an ADC for accomplishing effective therapeutic responses without compromising the affinity of the antibody [6,7]. Consequently, the drugs conjugated to the antibody must be highly cytotoxic, such as auristatins [8,9], maytansines [10,11] and calicheamicins [12], which are 100–1000 times higher than typical anticancer drugs, for exerting enough efficacy, although there are growing concerns over side effects from decomposition of ADC under physiological conditions [13,14]. However, these obstacles of ADCs may be overcome by integrating antibodies to drug-loaded nanocarriers, which are capable of delivering a significantly higher amount than ADCs [15].

Among long-circulating nanocarriers with improved tumor extravasation and penetration, polymeric micelles offer substantial benefits as platform nanocarriers for conjugating antibodies. Polymeric micelles present high and versatile loading of bioactive molecules and their controlled release, and show prolonged blood circulation (stealth property) due to their surface coverage by biocompatible PEG strands [16–19]. Besides the relative small size of micelles ranging from 10 to 100 nm, they exhibit enhanced

* Corresponding author. Department of Materials Engineering, Graduate School of Engineering, The University of Tokyo, 7-3-1 Hongo, Bunkyo-ku, Tokyo 113-8656, Japan. Tel.: +81 3 5841 7138; fax: +81 3 5841 7139.
E-mail address: kataoka@bmw.t.u-tokyo.ac.jp (K. Kataoka).

http://dx.doi.org/10.1016/j.biomaterials.2014.10.069
0142-9612/

tumor accumulation by the enhanced permeability and retention (EPR) effect through leaky vasculatures and impaired lymphatic drainage in solid tumors [20,21]. To date, a few antibody-conjugated micelles (immunomicelles) were reported for specific delivery of drugs in cancer therapy. One of the earliest immunomicelles were paclitaxel-loaded lipid-micelles conjugating nucleosome-targeting 2C5 antibody on their surface for specific targeting of breast adenocarcinoma and Lewis lung carcinoma [22,23]. Recently, epidermal growth factor receptor (EGFR)-targeting [24] and HER-2-targeting immunomicelles incorporating doxorubicin [25], and hypoxia inducible factor 1 (HIF-1)-targeting paclitaxel-loaded immunomicelles [26] have shown enhanced efficacy toward antigen-overexpressing cancer cells, indicating the high potential of immunomicelles in targeted cancer therapy. However, no immunomicelle has proceeded to clinical evaluation so far. Therefore, using micellar platform with high potential for clinical translation should facilitate the development of anticancer therapies based on immunomicelle.

Herein, we introduced the antibody fragments to polymeric micelles incorporating an active complex of oxaliplatin, (1,2-diaminocyclohexane)platinum(II) (DACHPt) (DACHPt/m), which have shown strong therapeutic activity against several cancer models and are being evaluated in phase I clinical studies [27]. DACHPt/m are self-assembled by the polymer-metal complex formation between the carboxylates of poly(glutamic acid) of poly(-ethylene glycol)-*b*-poly(glutamic acid) (PEG-*b*-P(Glu)) copolymers and the platinum drug [28]. The release of the incorporated DACHPt from the micelles is triggered by the ligand exchange of Pt(II) from the carboxylates in the block copolymer to chloride ions in the media, and is further accelerated at low pH conditions [29]. Accordingly, DACHPt/m stably circulate in the bloodstream in micelle form with minimal drug release, and after accumulating in tumor tissues and being endocytosed by cancer cells, the drug release from DACHPt/m is accelerated due the low pH and high chloride ion concentration of late endosomes/lysosomes. By conjugating antibody fragments to DACHPt/m, DACHPt/m could improve the efficacy of the loaded platinum drugs by enhanced delivery to tumor cells and effective intracellular drug release. In this regards, we may maximize therapeutic effects through antibody-antigen recognition and cellular uptake. As an antibody, we selected our recently developed anti-tissue factor (TF) antibody (clone 1849), which can target TF overexpressed on the surface of cancer cells, such as human pancreatic, colorectal, breast and lung cancers [30–32], as well as tumor associated monocytes and endothelial cells [31,33]. In fact, this anti-TF antibody demonstrated efficient targeting abilities including inhibition of the invasion and metastasis [34]. Accordingly, the development of these anti-human TF-antibody Fab' fragment-conjugated DACHPt/m (anti-TF Fab'-DACHPt/m) was studied in detail to determine their potential as a versatile target antigen for tumor-selective drug delivery. These immunomicelles were further evaluated against a tumor model of pancreatic cancer, because it is one of the most challenging models for drug delivery [35,36] and the application of antibody-antigen systems to polymeric micelles may positively impact on its clinical treatment. Our results highlight the potential of this approach for constructing Fab'-installed polymeric micelles for efficient drug delivery to tumors.

2. Materials and methods

2.1. Materials

α-Methoxy-ω-amino poly(ethylene glycol) (MeO-PEG-NH_2; M_n: 12,000), *N*-carboxyl anhydride of γ-Benzyl-L-glutamate (NCA-BLG) were purchased from NOF Co., Inc. (Tokyo, Japan) and Chuo Kaseihin Co., Inc. (Tokyo, Japan), respectively. Dimethyl formamide (DMF), dimethyl sulfoxide (DMSO), dithiothreitol (DTT), *N*-(4-Maleimidobutyryloxy)-sulfosuccinimide, sodium salt (Sulfo-GMBS), sodium sulfate decahydrate ($Na_2SO_4 \cdot 10H_2O$), oxaliplatin and phosphate buffered saline (PBS) were obtained from Wako Pure Chemical Co., Inc. (Osaka, Japan). MeO-PEG-*b*-P(Glu) was synthesized as previously described synthetic method [28]. MeO-PEG-*b*-P(Glu); yield = 97%, the degree of polymerization of the P(Glu) ($DP_{P(Glu)}$) = 40, $M_{n,NMR}$ = 18,000. ^{1}H NMR (400 MHz, D_2O): δ (ppm) = 1.70–2.55 (−C$\underline{H}_2$−C$\underline{H}_2$−P(Glu) side chain), 3.30 (−O−C$\underline{H}_3$), 3.45–3.85 (−C$\underline{H}_2$−C$\underline{H}_2$−O−PEG backbone), 4.20–4.40 (−C$\underline{H}$−P(Glu) backbone). Mal-PEG-*b*-P(Glu) was synthesized based on our previously reported method [37]. Mal-PEG-*b*-P(Glu); yield = 94%, $DP_{P(Glu)}$ = 40, ^{1}H NMR (400 MHz, D_2O): δ (ppm) = 1.70–2.65 (−C$\underline{H}_2$−C$\underline{H}_2$−P(Glu) side chain), 3.35 (−$(CH_2)_3$−CO−NH−C$\underline{H}_2$−), 3.50–3.92 (−C$\underline{H}_2$−C$\underline{H}_2$−O−PEG backbone), 4.12–4.46 (−C$\underline{H}$−P(Glu) backbone), 6.85 (−C$\underline{H}$=C$\underline{H}$− maleimide group). Dichloro(1,2-diaminocyclohexane)platinum(II) ($DACHPtCl_2$) was purchased from Heraeus (Hanau, Germany). $AgNO_3$ was purchased from Aldrich Chemical Co., Inc. (Milwaukee, WI). BCA protein assay reagent was purchased from Pierce Chemical Co., Inc. (Rockford, IL). Alexa Fluor 647-succinimidyl esters, Alexa Fluor 488-TFP ester, Hoechst 33342, and LysoTracker Green were purchased from Invitrogen Molecular Probes (Eugene, OR). Rhodamine 6G was purchased from Sigma–Aldrich Co., Inc. (St. Louis, MO). Anti-human tissue factor antibody (1849c, F(ab')$_2$) and anti-mouse tissue factor antibody (1157c, F(ab')$_2$) were purchased from ITM Co., Ltd. (Nagano, Japan). Fetal bovine serum (FBS) was purchased from Dainippon Sumitomo Pharma Co., Ltd. (Osaka, Japan). Cell Counting Kit-8 was obtained from Dojindo Laboratories (Kumamoto, Japan).

2.2. Cell lines and animals

Human pancreatic cancer BxPC3 cells were obtained from American Type Culture Collection (Manassas, VA). The BxPC3 cells were maintained in RPMI 1640 medium (Sigma Chemical Co., Inc., St. Louis, MO) supplemented with 10% (v/v) FBS, 1% penicillin/streptomycin in a humidified atmosphere containing 5% CO_2 at 37 °C. BALB/c nu/nu mice (18–20 g body weight; female; age, 6 weeks) were purchased from Charles River Japan (Kanagawa, Japan). All animal experiments were performed in accordance with the Guidelines for the Care and Use of Laboratory Animals as stated by the University of Tokyo.

2.3. Preparation of antibody fragment Fab' with thiols

To obtain Fab' fragment having thiol residues, F(ab')$_2$ fragments of anti-human TF antibody (0.5 mg/mL) were stirred with different concentrations of DTT from 0.5 μM to 5 mM for 30 min at 37 °C. The crude product was purified by ultrafiltration 4 times (MWCO: 30,000). The purity of Fab' fragment was confirmed by aqueous phase GPC (JASCO HPLC system, Easton, MD), which equipped with UV detector and a Superdex™ 200 10/300 GL column (GE healthcare, Ltd., Buckinghamshire, UK), with eluent of 10 mM phosphate buffer (pH 7.4) containing 150 mM NaCl at a flow rate of 0.75 mL/min at room temperature. For the fluorescence-labeling, anti-human TF F(ab')$_2$ (1 mg/mL) was combined with Alexa Fluor 488 in 1M $NaHCO_3$ solution at room temperature. After 1 h stirring, the Alexa 488-labeled F(ab')$_2$ was separated from non-conjugated free Alexa dye by PD-10 column. The labeled F(ab')$_2$ was then treated by DTT in the same manner as explained in above to afford Alexa 488-labeled anti-TF Fab' fragment having thiol residues.

2.4. Preparation and characterization of maleimide-functionalized DACHPt-loaded micelles (Mal-DACHPt/m)

MeO-PEG-*b*-P(Glu) and Mal-PEG-*b*-P(Glu) (total [Glu] = 5 mM) were mixed with $DACHPt(NO_3)Cl$ (5 mM) in distilled water at 37 °C, for preparation of 50% Mal-DACHPt/m [MeO-PEG-*b*-P(Glu)]/[Mal-PEG-*b*-P(Glu)] = 1.0/1.0 (mol/mol)] and 20% Mal-DACHPt/m [4.0/1.0 (mol/mol)]. The obtained micelles were purified by dialysis (Spectra/Pro 6 Membrane: MWCO: 6-8,000), followed by ultrafiltration (MWCO: 30,000) to afford Mal-DACHPt/m. The size and distribution of both Mal-DACHPt/m were estimated by dynamic light scattering (DLS: Malvern Instruments Ltd., UK, at 532 nm, 25 °C) measurement. The content of Pt in the micelles was measured by the inductively coupled plasma mass spectrometry (ICP-MS; Agilent 7700 series ICP-MS, Agilent Technologies, Inc., Santa Clara, CA). The association degree of Pt and carboxylic acid in P(Glu) was calculated by the Pt contents and freeze-dried weight of the micelles. Alexa 647-labeled Mal-DACHPt/m were obtained by using Alexa Fluor 647-labeled MeO-PEG-*b*-P(Glu) [37].

2.5. Preparation and characterization of antibody fragment-conjugated micelles

Anti-TF Fab' was conjugated to 50% Mal-DACHPt/m or 20% Mal-DACHPt/m by incubation at room temperature overnight to afford immunomicelles. Before the conjugation reaction, the concentration of antibody was determined by BCA protein assay kit with anti-TF Fab' antibody as the standard. The feed ratio between maleimide groups of Mal-DACHPt/m and anti-TF Fab' was 17.0/1.0 (mol/mol) for preparation of 50% Mal-DACHPt/m and 6.8/1.0 (mol/mol) for that of 20% Mal-DACHPt/m. The conjugation of antibody fragments to Mal-DACHPt/m was confirmed with fluorescence correlation spectroscopy using a Zeiss LSM 510 META equipped with FCS setup ConfoCor 3 (Carl Zeiss, Germany). The fluorescence of Alexa 488-labeled Fab' fragments was detected with a 488 nm Argon laser for excitation and a 530 nm band-pass filter for emission before and after the conjugation with non-fluorescence labeled 20% Mal-DACHPt/m or 50% Mal-DACHPt/m. After the

measurement, the diffusion time of Fab' fragments and immunomicelles were calculated from the autocorrelation curves. Diffusion coefficient was then calculated based on the diffusion times of micelles and Rhodamine 6G as standard fluorescence molecule.

2.6. In vitro evaluation of anti-TF Fab'-DACHPt/m by flow cytometry

Alexa 647 fluorescence-labeled anti-TF Fab'-DACHPt/m or DACHPt/m were added to BxPC3 cells (1×10^5 cells in 100 μL medium) and incubated at 4 °C for 1 h, without light exposure. Cells were washed four times with fresh medium to remove unbound micelles, resuspended in PBS and the mean fluorescence intensities were measured by flow cytometry (Becton Dickinson LSR II) and analyzed by BD FACSDiVa software. During the measurement, 10,000 events were counted per each sample. For the competition assay, the 10-fold excess of free anti-human TF $F(ab')_2$ fragments were co-incubated with Alexa 647-labeled anti-TF Fab'-DACHPt/m with BxPC3 cells, and the experiment was carried out as described above.

2.7. Assessment of cellular uptake by confocal laser scanning microscopy (CLSM)

The fluorescence intensity of micelles was adjusted to equal intensity by Nanodrop 3300 (RFU = 8,000). Alexa 647-labeled DACHPt/m or anti-TF Fab'-DACHPt/m were added to BxPC3 cells (1.6×10^4 cells in 200 μL medium) in Lab-Tek 8-well chambered coverglass (Thermo, Rochester, NY). After determined time periods, the cells were washed twice with fresh medium, stained with Hoechst 33342, and imaged with CLSM using a Zeiss LSM 780 (Carl Zeiss, Germany). The fluorescence was quantified by measuring the mean pixel intensities from Alexa 647-labeled micelles in cell areas using the LSM software ($n = 25$). The statistical significance of cellular uptake was determined by Student's *t*-test. By staining with LysoTracker Green, the colocalization of Alexa 647-labeled-anti-TF Fab'-DACHPt/m with late endosomal/lysosomal compartments was assessed.

2.8. In vitro cytotoxicity

The 50 percent inhibitory concentration (IC_{50}) of free oxaliplatin, DACHPt/m, anti-TF Fab'-DACHPt/m and anti-TF Fab' was evaluated by cytotoxicity assay against BxPC3 cells. The cells were exposed to the drugs for 3 h, followed by washing three times with fresh medium and post-incubated for 48 h. Then, the viability of cells was measured by using Cell Counting Kit-8. For the cytotoxicity evaluation of anti-TF Fab', the cells were continuously exposed to the antibody fragments for 48 h, and the viability of the cells was investigated as aforementioned.

2.9. In vivo antitumor activity assay on BxPC3 subcutaneous tumor model

To prepare BxPC3 subcutaneous xenografts, BALB/c nu/nu mice (6 week old, female) were inoculated with 5×10^6 cells. When the average tumor volume reached 50 mm^3, mice were i.v. injected from the tail vein at 3 times every fourth day with saline (PBS), oxaliplatin (8 mg/kg), DACHPt/m (3 mg/kg), anti-TF Fab'-DACHPt/m (3 mg/kg), and co-injection of Mal-DACHPt/m (3 mg/kg) and anti-TF Fab'. The tumor volume was measured by a caliper and calculated with the use of the following equation:

$$\text{Volume}_{\text{tumor}} = 0.5\ (\text{Major diameter}) \times (\text{Minor diameter})^2$$

The statistical significance of the antitumor activity was determined by Two-way ANOVA test.

2.10. Platinum accumulation on BxPC3 subcutaneous tumor in mouse xenograft

BxPC3 cells (5×10^6 cells in medium) were inoculated to BALB/c nu/nu mice (6 week old, $n = 5$, female) to establish subcutaneous BxPC3 tumor model. When the average tumor size is reached c.a. 100 mm^3, anti-TF Fab'-DACHPt/m, DACHPt/m and oxaliplatin were intravenously injected into the tail vein at 5 mg/kg on a DACHPt basis. Mice were sacrificed after 1, 6 and 24 h injection. Tumors were excised and decomposed with nitric acid on a hot plate until the samples became dried. Approximately 1.0 mL of nitric acid (1 vol%, 1.0 mL) was added to the samples to be dissolved, then the platinum concentration in the solution was measured by ICP-MS.

3. Results and discussion

3.1. Preparation of maleimide-functionalized DACHPt-loaded micelles

The block copolymers such as methoxy-poly(ethylene glycol)-*b*-poly(glutamic acid) (MeO-PEG-*b*-P(Glu), polymer 1 in Fig. 1) copolymer and maleimide-PEG-*b*-P(Glu) copolymer (Mal-PEG-*b*-P(Glu), polymer 2 in Fig. 1) were added to DACHPt aqueous solution to prepare the maleimide-functionalized DACHPt-loaded micelles (Mal-DACHPt/m) [37,38]. During this process, the coordinate covalent bonds occurred between the platinum atom and the carboxylate groups of poly(glutamic acid), and then triggered their self-assembling to form core-shell micelles, with DACHPt in their core and maleimide moieties on their PEG shell (Fig. 1) [28,39]. The proportion of maleimide functionality on the shell of micelles was controlled for optimizing the conjugation of antibody fragments by directly adjusting the ratio of polymer 1 and polymer 2. In this way, we prepared Mal-DACHPt/m with different maleimide density in the surface of micelle such as 20% Mal-DACHPt/m and 50% Mal-DACHPt/m. The diameter of these Mal-DACHPt/m was approximately 30 nm with narrow distribution, as determined by dynamic light scattering measurements (DLS), which was comparable to that of DACHPt/m prepared from MeO-PEG-*b*-P(Glu) (Table 1). The complexation ratio of Pt to carboxylate ([Pt]/[COO] = mol/mol) and the drug loading of Mal-DACHPt/m (Pt/polymer = wt/wt%) were also comparable to that of DACHPt/m (Table 1). The maleimide

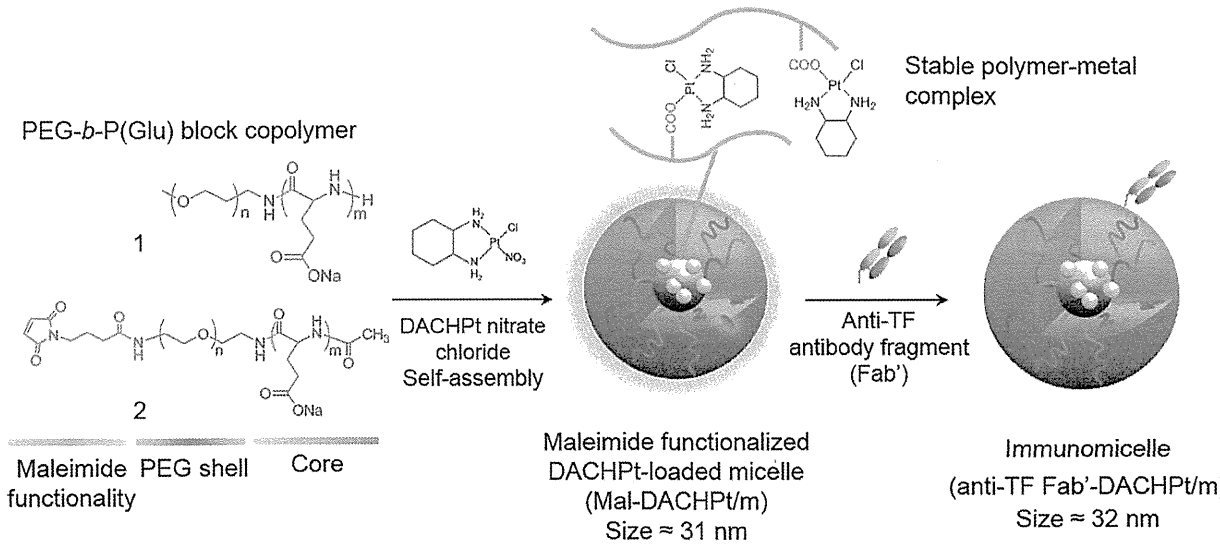

Fig. 1. Schematic illustration of the preparation of anti-TF Fab' fragment-installed DACHPt/m.

Table 1
Characterization of maleimide-functionalized DACHPt/m.

Micelles	Size [nm][a]	PDI[b]	[Pt]/[COO][c] [mol/mol]	Pt/polymer[c] [wt/wt%]
DACHPt/m	30	0.09	0.48	46
20% Mal-DACHPt/m	28	0.09	0.46	44
50% Mal-DACHPt/m	31	0.10	0.47	45
anti-TF Fab'-DACHPt/m[d]	32	0.17	0.45	44

[a] Volume averaged diameter determined by DLS.
[b] Polydispersity index determined by DLS.
[c] Determined by ICP-MS.
[d] Anti-TF Fab'-conjugated 50% Mal-DACHPt/m.

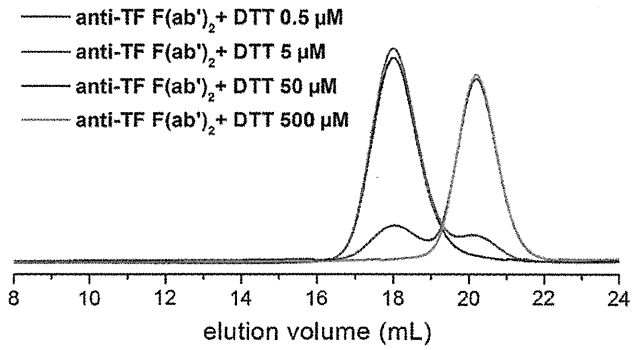

Fig. 2. GPC chromatograms detected by UV absorption at 220 nm of anti-TF F(ab')$_2$ fragment after DTT treatment with different concentrations.

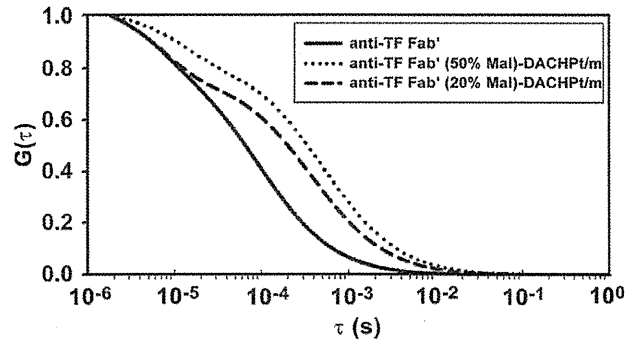

Fig. 3. FCS autocorrelation curves of Alexa 488-labeled anti-TF Fab' fragment before and after the conjugation with 20% Mal-DACHPt/m or 50% Mal-DACHPt/m.

groups on Mal-DACHPt/m allow introducing antibodies through thiol-maleimide reaction, which is a widely used linkage for preparing ADC [40,41]. Moreover, the conjugation of antibodies on the surface of micelles avoids the binding of platinum drugs with the

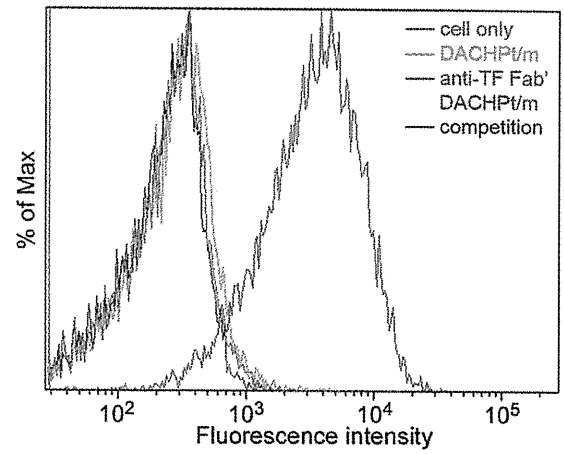

Fig. 4. Binding of Alexa 647-labeled DACHPt/m (green line) and anti-TF Fab'-DACHPt/m (blue line) against human pancreatic cancer BxPC3 cell after 1 h incubation at 4 °C analyzed by flow cytometry. Competition experiments on BxPC3 cells (black line) were performed by co-incubating anti-TF Fab'-DACHPt/m with 10-fold excess free anti-human TF F(ab')$_2$. The cells without any micelles were used as a negative control (red line).

antibodies, which may reduce their binding affinity, and eliminates the potential disturbance of the antibodies on the self-assembly process of the micelles. In addition, because the release of DACHPt from the core of micelles is induced by acidic pH and Cl^-, the conjugation of the antibodies by thiol-maleimide chemistry is a substantial advantage, as it can be performed in water without changing pH, preventing drug leakage [42,43]. Thus, these Mal-DACHPt/m could facilitate the efficient conjugation of antibodies without affecting their properties.

3.2. Conjugation of antibody fragments to maleimide-functionalized DACHPt/m

Thiol-bearing Fab' fragments of anti-human TF antibody (anti-TF Fab') were fabricated by cleaving the interchain disulfide bonds of F(ab')$_2$ through reduction with dithiothreitol (DTT), as these bonds are readily reducible sites, and their cleavage is frequently used for antibody conjugation without losing the binding properties of antibodies [40,43,44]. The optimal reduction conditions for preparing anti-TF Fab' were determined by gel permeation chromatography (GPC) (Fig. 2), following the shift of the peak related to F(ab')$_2$ at 18.0 min to that of anti-TF Fab' at 20.5 min. When 500 μM of DTT was added to the reaction system, we observed only the peak corresponding anti-TF Fab', while F(ab')$_2$ treated with 5 and 50 μM DTT showed the coexistence of F(ab')$_2$ and anti-TF Fab' (Fig. 2). It is worth noticing that, at DTT concentrations higher than 500 μM, Fab'

Table 2
FCS parameters of fluorescently labeled anti-TF Fab' before and after conjugation with Mal-DACHPt/m.

	Correlation[a]	Counts per molecule [kHz][a]	Diffusion time [μs][a]	Diffusion coefficient [μm^2/sec][a]	Hydrodynamic diameter [nm][b]
Anti-TF Fab'	1.03	3.61	92.4 ± 1.6	77.6 ± 1.3	6
Anti-TF Fab' (20% Mal)-DACHPt/m	1.02	2.51	437.1 ± 12.9	16.4 ± 0.5	27
Anti-TF Fab' (50% Mal)-DACHPt/m	1.03	3.66	505.3 ± 6.5	14.2 ± 0.2	31

[a] Correlation, counts per molecule and diffusion time were calculated by ConfoCor 3 software.
[b] Hydrodynamic diameter was calculated by Stokes-Einstein equation.

fragment decomposed into smaller fragments, showing the chromatograms at later elusion times (data not shown). Therefore, we concluded that 500 μM of DTT was the optimal concentration for producing anti-TF Fab'.

The obtained anti-TF Fab' were purified by ultrafiltration, followed by the installation on Mal-DACHPt/m through the formation of thioether bond [6,45]. The conjugation of anti-TF Fab' to Mal-DACHPt/m was studied by following the changes in the diffusion coefficient of Alexa 488-labeled anti-TF Fab' by fluorescence correlation spectroscopy (FCS). From the FCS autocorrelation function curves of Alexa 488-labeled anti-TF Fab' and its conjugated DACHPt/m (anti-TF Fab'-DACHPt/m) (Fig. 3), it was observed that the diffusion coefficient of anti-TF Fab'-DACHPt/m was significantly smaller than that of single anti-TF Fab' (Table 2), indicating the successful conjugation of anti-TF Fab' on Mal-DACHPt/m. In addition, the counts per molecule (CPM), *i.e.* the mean fluorescence intensity per molecule, in single anti-TF Fab' were comparable to that of 50% anti-TF Fab'-DACHPt/m (Table 2), suggesting that one anti-TF Fab' was conjugated to each 50% Mal-DACHPt/m in this reaction setting. The calculated CPM for anti-TF Fab'-DACHPt/m prepared from 20% Mal-DACHPt/m was less than that of single anti-TF Fab'. This implies that the anti-TF Fab'-DACHPt/m obtained from 20% Mal-DACHPt/m were a mixture of micelles with and without Fab'. Therefore, we selected 50% Mal-DACHPt/m for Fab' conjugation. The hydrodynamic diameter of Mal-DACHPt/m remained close to 30 nm even after Fab' conjugation (Tables 1 and 2). This might be reasonable considering the diameter of Fab' as that of a volume-equivalent sphere of 4–6 nm [46] (Table 2). This relatively small size of anti-TF Fab'-DACHPt/m could be a significant advantage for effective extravasation and penetration in stroma-rich tumor tissues of pancreatic cancer [35].

3.3. *Binding activity of anti-TF Fab'-DACHPt/m on TF-overexpressing human pancreatic cancer cells*

To study the binding of anti-TF Fab'-DACHPt/m to TF-expressing cells, human pancreatic cancer BxPC3 cells, which overexpress TF [47], were exposed to fluorescent-labeled anti-TF Fab'-DACHPt/m

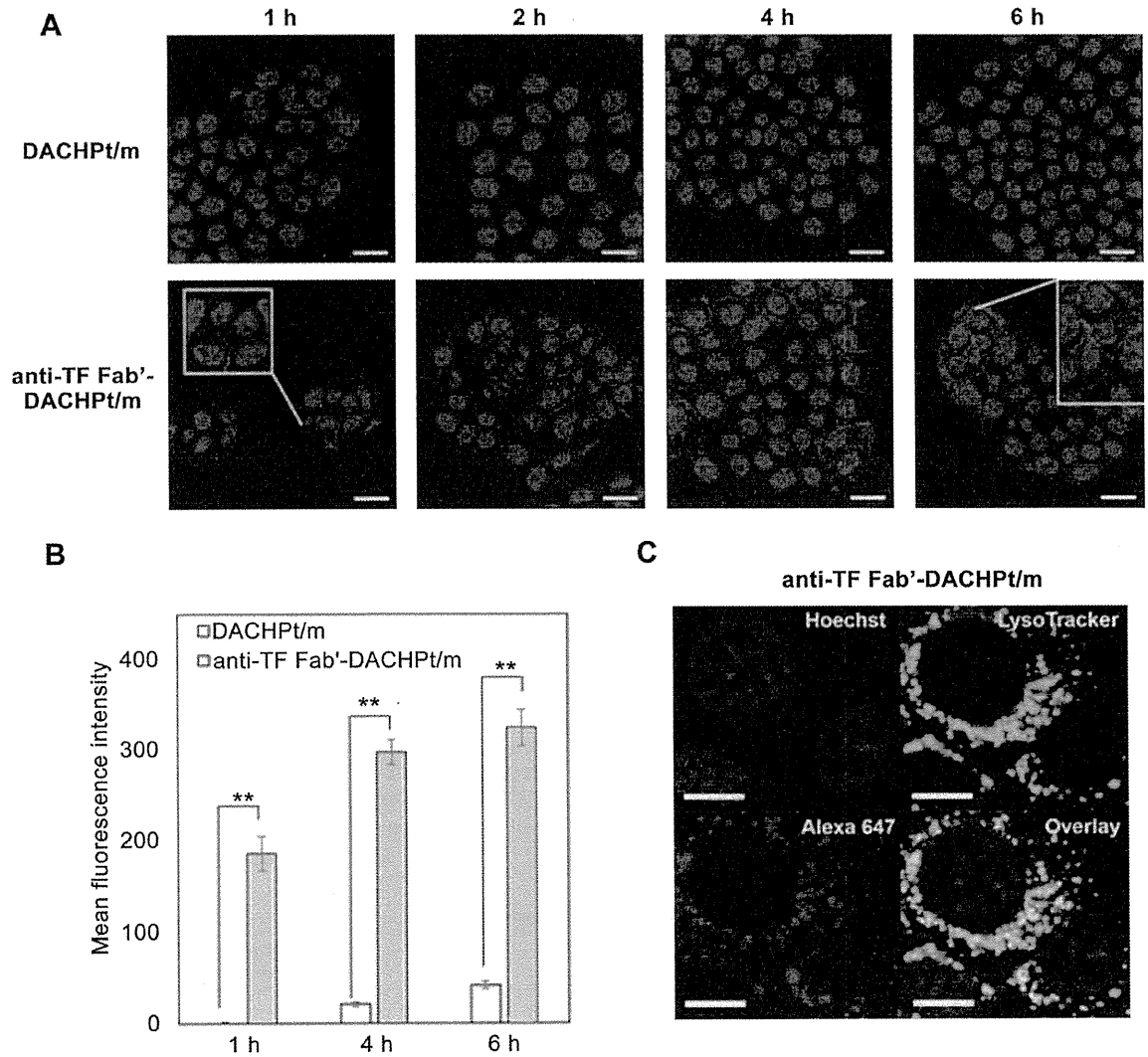

Fig. 5. (A) Representative CLSM images of BxPC3 cells incubated with Alexa 647-labeled DACHPt/m and anti-TF Fab'-DACHPt/m for 1–6 h at 37 °C. The merged images of Hoechst 33342-stained nuclei (blue) and fluorescence-labeled micelles (red) (scale bar = 20 μm); (B) The mean fluorescence intensity of Alexa 647 in BxPC3 cells from images taken at 1, 4, 6 h was quantified ($n = 25$, error bar = ±S.E.M., $^{**}p < 0.001$ calculated by Student's *t*-test); (C) Cellular localization of anti-TF Fab'-DACHPt/m after 6 h exposure against BxPC3 cells at 37 °C. The images show Alexa 647-labeled micelles (red), late endosomes and lysosomes stained by LysoTracker Green (green), nuclei stained by Hoechst 33342 (blue) and their overlay (scale bar = 10 μm).

Table 3
Concentration of drugs for fifty-percent inhibition of the growth of BxPC3 cells.

Cells	IC_{50} [μM][a]			
	Oxaliplatin	DACHPt/m	anti-TF Fab'-DACHPt/m	anti-TF Fab[b]
BxPC3	23	126	25	N/A

[a] Determined by CCK-8.
[b] Exposed for 48 h.

for 1 h at 4 °C. Then, the amount of micelles bound to the cells was assessed through flow cytometry. The average fluorescence levels in the cells treated with anti-TF Fab'-DACHPt/m (blue line) were more than 15-fold higher than control BxPC3 cells (red line) (Fig. 4), indicating the promoted cellular binding of these micelles after 1 h incubation, while DACHPt/m (green line) did not show any cellular binding. To confirm whether the enhanced cellular association of anti-TF Fab'-DACHPt/m results from the specific binding of anti-TF Fab' to TF on the cell surface, a competition experiment was performed by using 10-fold excess amount of free anti-human TF $F(ab')_2$. The results demonstrated that the cells treated by anti-TF Fab'-DACHPt/m and excess anti-human TF $F(ab')_2$ (Fig. 4; black line) did not show any increase in the fluorescence levels. It is likely that TF on BxPC3 cells were occupied by the excess free $F(ab')_2$, thereby restricting the binding sites for anti-TF Fab'-DACHPt/m. From these results, we concluded that the introduced anti-TF Fab' on DACHPt/m can selectively bind to TF overexpressed on BxPC3 cells. It is worth noting that only one anti-TF Fab' conjugation to each micelle promoted such enhanced binding.

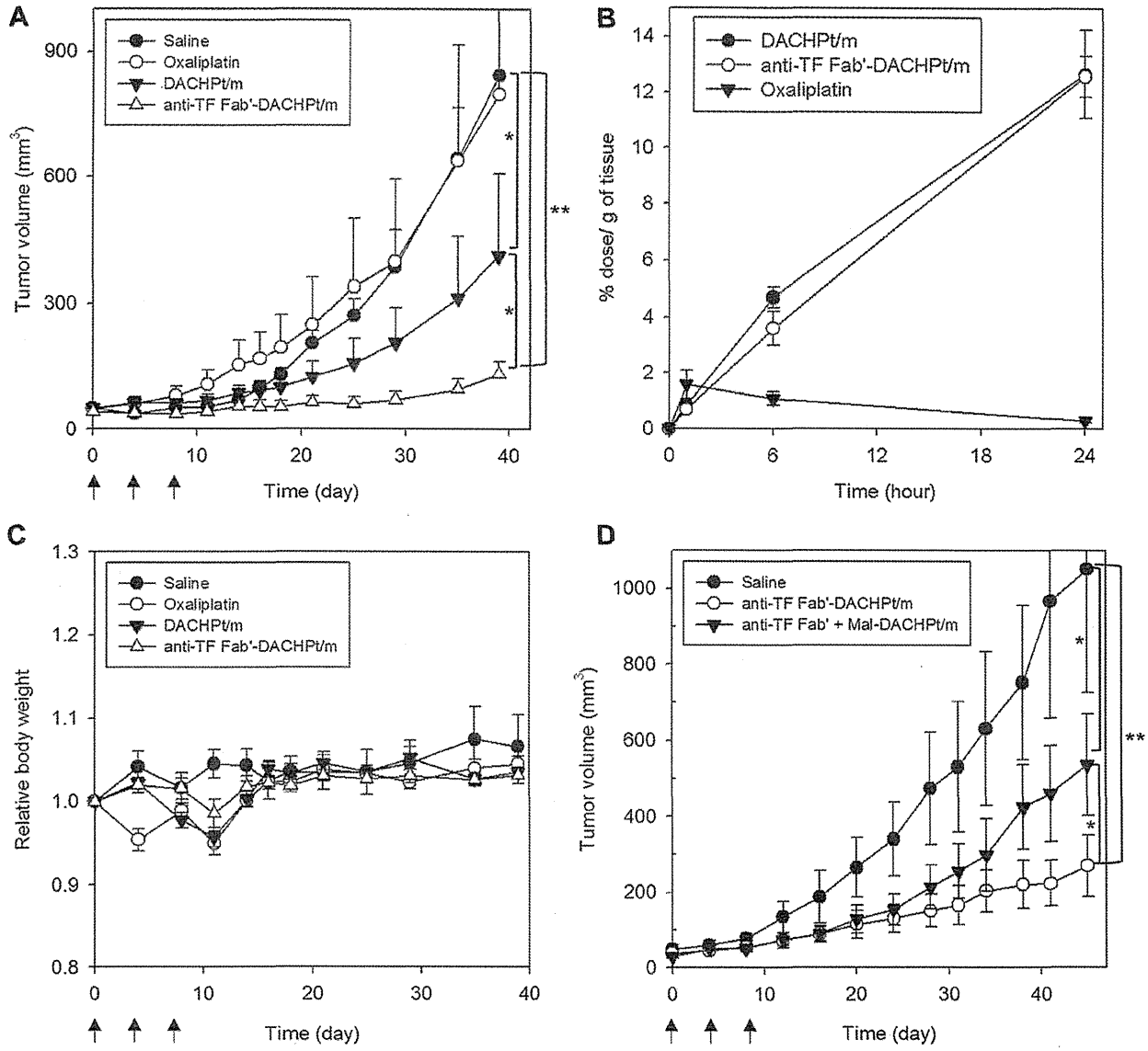

Fig. 6. *In vivo* antitumor efficacy of DACHPt/m series against human pancreatic adenocarcinoma BxPC3 xenografts. (A) The drugs were injected three times as indicated with arrows, every 4th day from day 0 (*$p < 0.01$, **$p < 0.001$ calculated by Two-way ANOVA, Error bars = S.E.M.; $n = 5$). The doses for DACHPt/m and anti-TF Fab'-DACHPt/m were 3 mg/kg on a DACHPt basis, and oxaliplatin for 8 mg/kg; (B) Time profiles of Pt concentration in tumor after i.v. administration into BALB/c nude mice bearing BxPC3 subcutaneous tumor ($n = 5$). The doses for DACHPt/m, anti-TF Fab'-DACHPt/m and oxaliplatin were 5 mg/kg on a DACHPt basis. Error bars = S.E.M.; (C) Relative body weight of the mice during the antitumor activity experiment (A); (D) The doses for co-injection of anti-TF Fab' and Mal-DACHPt/m (anti-TF Fab' + Mal-DACHPt/m) and anti-TF Fab'-DACHPt/m were 3 mg/kg on a DACHPt basis (*$p < 0.01$, **$p < 0.001$ calculated by Two-way ANOVA, Error bars = S.E.M.; $n = 5$).

3.4. Cellular uptake and in vitro cytotoxicity

To confirm cellular internalization of anti-TF Fab' DACHPt/m in BxPC3 cells, we performed confocal laser scanning microscopy (CLSM) evaluation with fluorescence-labeled anti-TF Fab'-DACHPt/m and DACHPt/m (Fig. 5). After 1 h incubation, the fluorescence signal from anti-TF Fab'-DACHPt/m was clearly observed in BxPC3 cells, while DACHPt/m were barely discernable (Fig. 5A). From 2 h to 6 h incubation, the red fluorescence signal (anti-TF Fab'-DACHPt/m) was gradually increased, whereas the fluorescent signal from DACHPt/m was still significantly weak (Fig. 5A). Quantification of fluorescent intensity clearly indicated the rapid binding and internalization of anti-TF Fab'-DACHPt/m against BxPC3 cells (Fig. 5B). By staining the late endosomes and lysosomes with LysoTracker Green (Fig. 5C; green), we confirmed the colocalization (Fig. 5C; yellow) of anti-TF Fab'-DACHPt/m (Fig. 5C; red) and late endosomes/lysosomes in BxPC3 cells, suggesting that anti-TF Fab' promoted cellular uptake. This is in good agreement with previous reports regarding the TF-targeted ADC [47].

The *in vitro* cytotoxicity of anti-TF Fab'-DACHPt/m was studied in BxPC3 cells by exposing to anti-TF Fab'-DACHPt/m, DACHPt/m and oxaliplatin, which is the clinically approved derivative of DACHPt, for 3 h followed by post-incubation for 48 h. The 50% inhibitory concentrations (IC_{50}) of the drugs are summarized in Table 3. The IC_{50} value of DACHPt/m was higher than that of oxaliplatin, as free oxaliplatin is rapidly transported and activated inside the cells, while DACHPt/m are gradually internalized by the endocytosis and sustainedly release cytotoxic Pt complexes [29]. Nevertheless, the IC_{50} value of anti-TF Fab'-DACHPt/m was comparable to that of oxaliplatin, *i.e.* approximately 6-fold lower than that of DACHPt/m. It is worthy of note that, anti-TF Fab' did not show any *in vitro* cytotoxicity against BxPC3 cells under the tested conditions, indicating that the cytotoxicity of anti-TF Fab'-DACHPt/m can be attributed exclusively to the enhanced intracellular delivery of cytotoxic DACHPt. The internalized anti-TF Fab'-DACHPt/m colocalized with late endosomes/lysosomes of BxPC3 (Fig. 5C), which may result in the accelerated release of DACHPt from the anti-TF Fab'-DACHPt/m due to the low pH and high chloride ion concentration of late endosomal and lysosomal compartments [28,29]. Consequently, these results support that, the introduction of anti-TF Fab' on the surface of DACHPt/m may contribute to the substantial improvement of the *in vitro* cytotoxicity through the combination of i) promoted cellular uptake to TF-overexpressing cancer cells (Fig. 5A) and ii) subsequent efficient intracellular delivery of DACHPt *via* endocytosis (Fig. 5C).

3.5. In vivo antitumor efficacy and tumor accumulation of anti-TF Fab'-DACHPt/m

Encouraged by the high *in vitro* cytotoxicity of anti-TF Fab'-DACHPt/m against pancreatic cancer BxPC3 cells, we evaluated the *in vivo* antitumor activity against subcutaneous BxPC3 xenografts. Both DACHPt/m and anti-TF Fab'-DACHPt/m at 3 mg/kg showed enhanced antitumor effect compared to oxaliplatin at 8 mg/kg ($p < 0.001$ and $p < 0.01$, respectively). Particularly, anti-TF Fab'-DACHPt/m suppressed the growth of tumors for approximately 40 days ($p < 0.01$), outperforming DACHPt/m (Fig. 6A). It is worth mentioning that, even though BxPC3 xenografts present characteristics of intractable pancreatic cancer, including poor vascularization, perycite-covered vasculature and thick fibrosis, which impede the access of therapeutic agents [48–50], polymeric micelles with the size smaller than 50 nm showed facilitated penetration and accumulation in this tumor model [35]. Both DACHPt/m and anti-TF Fab'-DACHPt/m showed similar accumulation in tumor tissues (Fig. 6B), which is well-consistent with previously reported antibody-linked nanoparticles [51], indicating that the improved antitumor efficacy of anti-TF Fab'-DACHPt/m did not result from enhanced tumor accumulation. Instead, it is reasonable to assume that the prolonged antitumor efficacy achieved by anti-TF Fab'-DACHPt/m is attributed to the facilitated cellular uptake by TF-targeting (Fig. 5) and the resulting improvement of the cytotoxicity against BxPC3 cells (Table 3). Moreover, at the assessed dosage, neither DACHPt/m nor anti-TF Fab'-DACHPt/m were toxic according to the body weight profile (Fig. 6C). In addition, co-injection of anti-TF Fab' and Mal-DACHPt/m resulted in lower antitumor activity than anti-TF Fab'-DACHPt/m (Fig. 6D; $p < 0.01$), indicating that anti-TF Fab' may not exert any antitumor effect at the applied dose and that the thiol-maleimide conjugation of anti-TF Fab' on the micelles was an effective strategy for enhancing drug delivery.

4. Conclusions

In the present study, we designed and synthesized the DACHPt-incorporated polymeric micelle equipped with anti-human TF-targetable Fab' fragment on their surface, and demonstrated the feasibility of antitumor efficacy against stroma-rich intractable pancreatic tumors. The utilization of maleimide-thiol chemistry allowed the successful preparation of anti-TF Fab'-DACHPt/m with one-to-one tailored conjugation. Compared with DACHPt/m, antigen-recognition ability of anti-TF Fab' facilitated rapid cellular binding and internalization of anti-TF Fab'-DACHPt/m. Enhanced antitumor efficacy of anti-TF Fab'-DACHPt/m without impairing the safety of parent micelles, as at least suggested from the negligible loss in the body weight of treated mice, confirmed the advantages of *in vivo* tumor targeting by immunomicellar system loaded with platinum drugs, which are key drugs for many clinical anticancer therapies, for the first time. This strategy of one-to-one conjugation of Fab' fragment of antibody to polymeric micellar surface by maleimide-thiol coupling is applicable to a broad variety of cargo molecules and antibodies, including clinically approved tumor-directed antibodies, without substantial change in the structure and the size of parent micelles. Hence, it should provide a universality to deliver therapeutic agents into stroma-rich intractable tumors with strict limitation in extravasation of carrier systems, including pancreatic tumor as reported here, and enhance their therapeutic efficacy.

Acknowledgments

The authors thank R. Shiratori and N. Henzan for helping with synthesis experiments, Y. Mochida for micelle characterization, and K. Date for assistance with animal experiments. The authors also thank M. Naito for FCS analysis. This work was supported by the Funding Program for World-Leading Innovative R&D on Science and Technology (FIRST Program) from the Japan Society for the Promotion of Science (JSPS) (KK), Grants-in-Aid for Scientific Research from the Japanese Ministry of Health, Labor, and Welfare (MHLW) (NN, KK), and Center of Innovation Program (COI) from the Ministry of Education, Culture, Sports, Science and Technology (MEXT) (KK). This study was partially supported by Grants-in-Aid for Young Scientists (B; No. 23700526 and No. 25750172 to HC; and A; No. 24689051 to YM), Challenging Exploratory Research (No. 24659584 to YM), Initiative for Accelerating Regulatory Science in Innovative Drug, Medical Device, and Regenerative Medicine (KK), the National Cancer Center Research and Development Fund (YM) and the Health and Labour Sciences Research Grants (Clinical Trial on Development of New Drugs and Medical Devices) (YM).

References

[1] Trail P. Antibody drug conjugates as cancer therapeutics. Antibodies 2013;2:113–29.

[2] Flygare JA, Pillow TH, Aristoff P. Antibody-drug conjugates for the treatment of cancer. Chem Biol Drug Des 2013;81:113–21.
[3] Mullard A. Maturing antibody-drug conjugate pipeline hits 30. Nat Rev Drug Discov 2013;12:329–32.
[4] McDonagh CF, Turcott E, Westendorf L, Webster JB, Alley SC, Kim K, et al. Engineered antibody–drug conjugates with defined sites and stoichiometries of drug attachment. Protein Eng Des Sel 2006;19:299–307.
[5] Shen BQ, Xu K, Liu L, Raab H, Bhakta S, Kenrick M, et al. Conjugation site modulates the in vivo stability and therapeutic activity of antibody-drug conjugates. Nat Biotechnol 2012;30:184–9.
[6] Senter PD, Sievers EL. The discovery and development of brentuximab vedotin for use in relapsed Hodgkin lymphoma and systemic anaplastic large cell lymphoma. Nat Biotechnol 2012;30:631–7.
[7] Hamblett KJ, Senter PD, Chace DF, Sun MM, Lenox J, Cerveny CG, et al. Effects of drug loading on the antitumor activity of a monoclonal antibody drug conjugate. Clin Cancer Res 2004;10:7063–70.
[8] Doronina SO, Toki BE, Torgov MY, Mendelsohn BA, Cerveny CG, Chace DF, et al. Development of potent monoclonal antibody auristatin conjugates for cancer therapy. Nat Biotechnol 2003;21:778–84.
[9] Junutula JR, Raab H, Clark S, Bhakta S, Leipold DD, Weir S, et al. Site-specific conjugation of a cytotoxic drug to an antibody improves the therapeutic index. Nat Biotechnol 2008;26:925–32.
[10] Lewis Phillips GD, Li G, Dugger DL, Crocker LM, Parsons KL, Mai E, et al. Targeting HER2-positive breast cancer with trastuzumab-DM1, an antibody-cytotoxic drug conjugate. Cancer Res 2008;68:9280–90.
[11] LoRusso PM, Weiss D, Guardino E, Girish S, Sliwkowski MX. Trastuzumab emtansine: a unique antibody-drug conjugate in development for human epidermal growth factor receptor 2-positive cancer. Clin Cancer Res 2011;17:6437–47.
[12] Sievers EL, Senter PD. Antibody-drug conjugates in cancer therapy. Annu Rev Med 2013;64:15–29.
[13] Ducry L, Stump B. Antibody-drug conjugates: linking cytotoxic payloads to monoclonal antibodies. Bioconjug Chem 2010;21:5–13.
[14] Wu AM, Senter PD. Arming antibodies: prospects and challenges for immunoconjugates. Nat Biotechnol 2005;23:1137–46.
[15] Yokoyama M, Inoue S, Kataoka K, Yui N, Okano T, Sakurai Y. Molecular design for missile drug: synthesis of adriamycin conjugated with immunoglobulin G using poly(ethylene glycol)-block-poly(aspartic acid) as intermediate carrier. Makromol Chem 1989;190:2041–54.
[16] Aliabadi HM, Lavasanifar A. Polymeric micelles for drug delivery. Expert Opin Drug Deliv 2006;3:139–62.
[17] Kataoka K, Harada A, Nagasaki Y. Block copolymer micelles for drug delivery: design, characterization and biological significance. Adv Drug Deliv Rev 2001;47:113–31.
[18] Nishiyama N, Kataoka K. Current state, achievements, and future prospects of polymeric micelles as nanocarriers for drug and gene delivery. Pharmacol Ther 2006;112:630–48.
[19] Osada K, Christie RJ, Kataoka K. Polymeric micelles from poly(ethylene glycol)-poly(amino acid) block copolymer for drug and gene delivery. J R Soc Interface 2009;6(Suppl. 3):S325–39.
[20] Greish K. Enhanced permeability and retention (EPR) effect for anticancer nanomedicine drug targeting. Methods Mol Biol 2010;624:25–37.
[21] Matsumura Y, Maeda H. A new concept for macromolecular therapeutics in cancer chemotherapy: mechanism of tumoritropic accumulation of proteins and the antitumor agent smancs. Cancer Res 1986;46:6387–92.
[22] Gao Z, Lukyanov AN, Chakilam AR, Torchilin VP. PEG-PE/phosphatidylcholine mixed immunomicelles specifically deliver encapsulated taxol to tumor cells of different origin and promote their efficient killing. J Drug Target 2003;11:87–92.
[23] Torchilin VP, Lukyanov AN, Gao Z, Papahadjopoulos-Sternberg B. Immunomicelles: targeted pharmaceutical carriers for poorly soluble drugs. Proc Natl Acad Sci U S A 2003;100:6039–44.
[24] Noh T, Kook YH, Park C, Youn H, Kim H, Oh ET, et al. Block copolymer micelles conjugated with anti-EGFR antibody for targeted delivery of anticancer drug. J Polym Sci Pol Chem 2008;46:7321–31.
[25] Li W, Zhao H, Qian W, Li H, Zhang L, Ye Z, et al. Chemotherapy for gastric cancer by finely tailoring anti-Her2 anchored dual targeting immunomicelles. Biomaterials 2012;33:5349–62.
[26] Song H, He R, Wang K, Ruan J, Bao C, Li N, et al. Anti-HIF-1alpha antibody-conjugated pluronic triblock copolymers encapsulated with paclitaxel for tumor targeting therapy. Biomaterials 2010;31:2302–12.
[27] Cabral H, Kataoka K. Progress of drug-loaded polymeric micelles into clinical studies. J Control Release 2014;190:465–76.
[28] Cabral H, Nishiyama N, Okazaki S, Koyama H, Kataoka K. Preparation and biological properties of dichloro(1,2-diaminocyclohexane)platinum(II) (DACHPt)-loaded polymeric micelles. J Control Release 2005;101:223–32.
[29] Murakami M, Cabral H, Matsumoto Y, Wu S, Kano MR, Yamori T, et al. Improving drug potency and efficacy by nanocarrier-mediated subcellular targeting. Sci Transl Med 2011;3. 64ra2.
[30] Nitori N, Ino Y, Nakanishi Y, Yamada T, Honda K, Yanagihara K, et al. Prognostic significance of tissue factor in pancreatic ductal adenocarcinoma. Clin Cancer Res 2005;11:2531–9.
[31] van den Berg YW, Osanto S, Reitsma PH, Versteeg HH. The relationship between tissue factor and cancer progression: insights from bench and bedside. Blood 2012;119:924–32.
[32] Cole M, Bromberg M. Tissue factor as a novel target for treatment of breast cancer. Oncologist 2013;18:14–8.
[33] Lorenzet R, Napoleone E, Celi A, Pellegrini G, Di Santo A. Cell-cell interaction and tissue factor expression. Blood Coagul Fibrinolysis 1998;9:S49–59.
[34] Saito Y, Hashimoto Y, Kuroda J-i, Yasunaga M, Koga Y, Takahashi A, et al. The inhibition of pancreatic cancer invasion-metastasis cascade in both cellular signal and blood coagulation cascade of tissue factor by its neutralisation antibody. Eur J Cancer 2011;47:2230–9.
[35] Cabral H, Matsumoto Y, Mizuno K, Chen Q, Murakami M, Kimura M, et al. Accumulation of sub-100 nm polymeric micelles in poorly permeable tumours depends on size. Nat Nanotechnol 2011;6:815–23.
[36] Kano MR, Bae Y, Iwata C, Morishita Y, Yashiro M, Oka M, et al. Improvement of cancer-targeting therapy, using nanocarriers for intractable solid tumors by inhibition of TGF-beta signaling. Proc Natl Acad Sci U S A 2007;104:3460–5.
[37] Miura Y, Takenaka T, Toh K, Wu S, Nishihara H, Kano MR, et al. Cyclic RGD-linked polymeric micelles for targeted delivery of platinum anticancer drugs to glioblastoma through the blood-brain tumor barrier. ACS Nano 2013;7:8583–92.
[38] Cabral H, Nishiyama N, Kataoka K. Optimization of (1,2-diamino-cyclohexane) platinum(II)-loaded polymeric micelles directed to improved tumor targeting and enhanced antitumor activity. J Control Release 2007;121:146–55.
[39] Mochida Y, Cabral H, Miura Y, Albertini F, Fukushima S, Osada K, et al. Bundled assembly of helical nanostructures in polymeric micelles loaded with platinum drugs enhancing therapeutic efficiency against pancreatic tumor. ACS Nano 2014;8:6724–38.
[40] Alley SC, Benjamin DR, Jeffrey SC, Okeley NM, Meyer DL, Sanderson RJ, et al. Contribution of linker stability to the activities of anticancer immunoconjugates. Bioconjug Chem 2008;19:759–65.
[41] Erickson HK, Park PU, Widdison WC, Kovtun YV, Garrett LM, Hoffman K, et al. Antibody-maytansinoid conjugates are activated in targeted cancer cells by lysosomal degradation and linker-dependent intracellular processing. Cancer Res 2006;66:4426–33.
[42] Humphreys DP, Heywood SP, Henry A, Ait-Lhadj L, Antoniw P, Palframan R, et al. Alternative antibody Fab' fragment PEGylation strategies: combination of strong reducing agents, disruption of the interchain disulphide bond and disulphide engineering. Protein Eng Des Sel 2007;20:227–34.
[43] Song HY, Ngai MH, Song ZY, MacAry PA, Hobley J, Lear MJ. Practical synthesis of maleimides and coumarin-linked probes for protein and antibody labelling via reduction of native disulfides. J Org Biomol Chem 2009;7:3400–6.
[44] Thorpe PE, Wallace PM, Knowles PP, Relf MG, Brown AN, Watson GJ, et al. New coupling agents for the synthesis of immunotoxins containing a hindered disulfide bond with improved stability in vivo. Cancer Res 1987;47:5924–31.
[45] Barginear MF, Budman DR. Trastuzumab-DM1: a review of the novel immuno-conjugate for her2-overexpressing breast cancer. Open Breast Cancer J 2009;1:25–30.
[46] Chu TW, Yang J, Kopecek J. Anti-CD20 multivalent HPMA copolymer-Fab' conjugates for the direct induction of apoptosis. Biomaterials 2012;33:7174–81.
[47] Breij EC, de Goeij BE, Verploegen S, Schuurhuis DH, Amirkhosravi A, Francis J, et al. An antibody-drug conjugate that targets tissue factor exhibits potent therapeutic activity against a broad range of solid tumors. Cancer Res 2014;74:1214–26.
[48] Sofuni A, Iijima H, Moriyasu F, Nakayama D, Shimizu M, Nakamura K, et al. Differential diagnosis of pancreatic tumors using ultrasound contrast imaging. J Gastroenterol 2005;40:518–25.
[49] Kano MR, Komuta Y, Iwata C, Oka M, Shirai Y-t, Morishita Y, et al. Comparison of the effects of the kinase inhibitors imatinib, sorafenib, and transforming growth factor-β receptor inhibitor on extravasation of nanoparticles from neovasculature. Cancer Sci 2009;100:173–80.
[50] Dirisala A, Osada K, Chen Q, Tockary TA, Machitani K, Osawa S, et al. Optimized rod length of polyplex micelles for maximizing transfection efficiency and their performance in systemic gene therapy against stroma-rich pancreatic tumors. Biomaterials 2014;35:5359–68.
[51] Kirpotin DB, Drummond DC, Shao Y, Shalaby MR, Hong K, Nielsen UB, et al. Antibody targeting of long-circulating lipidic nanoparticles does not increase tumor localization but does increase internalization in animal models. Cancer Res 2006;66:6732–40.

Precise Engineering of siRNA Delivery Vehicles to Tumors Using Polyion Complexes and Gold Nanoparticles

Hyun Jin Kim,[†] Hiroyasu Takemoto,[‡] Yu Yi,[§] Meng Zheng,[⊥] Yoshinori Maeda,[§] Hiroyuki Chaya,[⊥] Kotaro Hayashi,[§] Peng Mi,[‡] Frederico Pittella,[⊥] R. James Christie,[⊥] Kazuko Toh,[⊥] Yu Matsumoto,[⊥] Nobuhiro Nishiyama,[‡] Kanjiro Miyata,[⊥,*] and Kazunori Kataoka[†,§,⊥,∥,*]

[†]Department of Materials Engineering, Graduate School of Engineering, The University of Tokyo, Tokyo 113-8656, Japan, [‡]Polymer Chemistry Division, Chemical Resources Laboratory, Tokyo Institute of Technology, Yokohama 226-8503, Japan, [§]Department of Bioengineering, Graduate School of Engineering, The University of Tokyo, Tokyo 113-8656, Japan, [⊥]Center for Disease Biology and Integrative Medicine, Graduate School of Medicine, The University of Tokyo, Tokyo 113-0033, Japan, and [∥]Center for NanoBio Integration, The University of Tokyo, Tokyo 113-8656, Japan

ABSTRACT For systemic delivery of siRNA to solid tumors, a size-regulated and reversibly stabilized nanoarchitecture was constructed by using a 20 kDa siRNA-loaded unimer polyion complex (uPIC) and 20 nm gold nanoparticle (AuNP). The uPIC was selectively prepared by charge-matched polyionic complexation of a poly(ethylene glycol)-*b*-poly(L-lysine) (PEG-PLL) copolymer bearing ~40 positive charges (and thiol group at the ω-end) with a single siRNA bearing 40 negative charges. The thiol group at the ω-end of PEG-PLL further enabled successful conjugation of the uPICs onto the single AuNP through coordinate bonding, generating a nanoarchitecture (uPIC-AuNP) with a size of 38 nm and a narrow size distribution. In contrast, mixing thiolated PEG-PLLs and AuNPs produced a large aggregate in the absence of siRNA, suggesting the essential role of the preformed uPIC in the formation of nanoarchitecture. The smart uPIC-AuNPs were stable in serum-containing media and more resistant against heparin-induced counter polyanion exchange, compared to uPICs alone. On the other hand, the treatment of uPIC-AuNPs with an intracellular concentration of glutathione substantially compromised their stability and triggered the release of siRNA, demonstrating the reversible stability of these nanoarchitectures relative to thiol exchange and negatively charged AuNP surface. The uPIC-AuNPs efficiently delivered siRNA into cultured cancer cells, facilitating significant sequence-specific gene silencing without cytotoxicity. Systemically administered uPIC-AuNPs showed appreciably longer blood circulation time compared to controls, *i.e.*, bare AuNPs and uPICs, indicating that the conjugation of uPICs onto AuNP was crucial for enhancing blood circulation time. Finally, the uPIC-AuNPs efficiently accumulated in a subcutaneously inoculated luciferase-expressing cervical cancer (HeLa-Luc) model and achieved significant luciferase gene silencing in the tumor tissue. These results demonstrate the strong potential of uPIC-AuNP nanoarchitectures for systemic siRNA delivery to solid tumors.

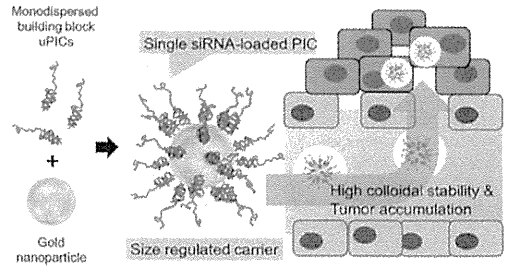

KEYWORDS: siRNA delivery · unimer polyion complex · gold nanoparticle · cancer therapy

Small interfering RNA (siRNA), which induces the sequence-specific degradation of mRNA in the cytoplasm (termed RNA interference (RNAi)), has attracted much attention in cancer therapy.[1,2] However, systemically administered siRNA is rapidly degraded by RNases in the bloodstream and/or eliminated through kidney filtration because they are smaller than 6 nm.[3,4] Thus, siRNA carriers need to be developed in order to overcome these issues for successful therapy. A variety of synthetic nanocarriers have been constructed mainly with cationic nanomaterials, such as lipids, polycations, inorganic nanoparticles, and their hybrid systems.[5−10] These nanocarriers can protect siRNA from enzymatic degradations and apparently increase its size to circumvent kidney filtration. This allows the siRNA payloads to accumulate in tumor tissues through the leaky tumor vasculature *via* the so-called enhanced permeability and retention (EPR) effect.[11,12] In this regard, several recent studies have revealed that precise size-tuning promotes the selective accumulation of nanoparticles in tumor tissues.[13,14] Nanoparticles with a size that is smaller than 50 nm can efficiently

* Address correspondence to kataoka@bmw.t.u-tokyo.ac.jp, miyata@bmw.t.u-tokyo.ac.jp.

Received for review April 17, 2014 and accepted August 18, 2014.

Published online August 18, 2014
10.1021/nn502125h

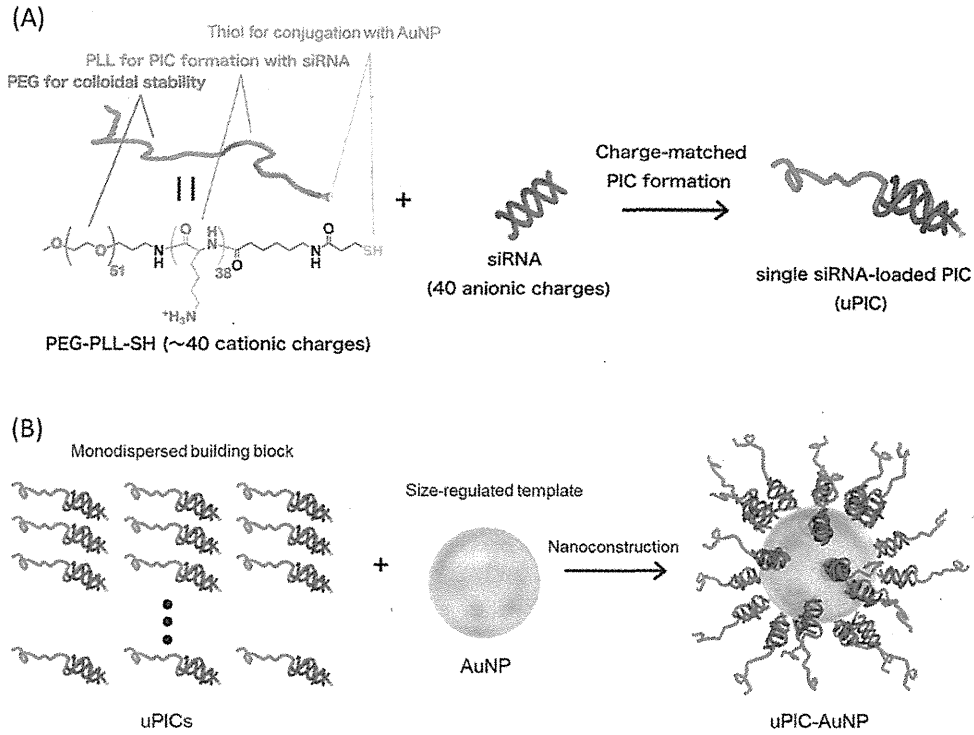

Figure 1. Schematic illustration showing the nanoconstruction of uPIC-AuNPs from monodispersed building blocks. (A) Formation of uPICs comprising a single pair of PEG-PLL and siRNA. (B) Thiol-gold coordination complex between uPICs and AuNP.

accumulate in tumor tissues, especially in a poorly permeable pancreatic tumor model.[13] Thus, the size of nanocarriers is important for enhancing siRNA accumulation in a variety of tumor tissues.

While multimolecular self-assemblies of siRNA with oppositely charged nanomaterials have been widely developed because of their facile and efficient encapsulation of siRNA, it is difficult to control the size and the distribution of these carriers. In contrast, the bottom-up nanocarrier construction with monodispersed building blocks and a nanotemplate enables more precise size-tuning at the nanoscale. With regard to such building blocks, our recent study demonstrated that a block copolymer of poly(ethylene glycol) and poly(L-lysine) (PEG-PLL) with a controlled degree of polymerization of PLL (DP_{PLL}) formed a unimer polyion complex (uPIC)[15] comprising a single siRNA molecule,[16,17] potentially serving as a monodispersed building block. A building-block-loading nanotemplate is necessary to satisfy the Janus-type property requirement for the selective siRNA release into the cytosol. Gold nanoparticles (AuNPs) are promising biocompatible nanotemplates, as their size can be precisely controlled with a narrow distribution, and also they can be coated with polymers or biomolecules through thiol chemistry.[18,19] This type of bonding is relatively stable under extracellular conditions, but these polymers or biomolecules can be competed off the AuNP with glutathione (GSH), which is abundant in the cytosol.[20] Subsequently, the GSH-coordinated anionic AuNPs may interact with uPICs to destabilize them for triggered siRNA release.

To achieve an efficient systemic siRNA delivery to solid tumors, we developed a size-regulated and reversibly stabilized nanoarchitecture (uPIC-AuNP) by utilizing an AuNP template and a monodispersed uPIC building block prepared with a single siRNA/PEG-PLL pair (Figure 1). To this end, a PEG-PLL was prepared to have a DP_{PLL} of ~40 (matched with the negative charges of 21mer/21mer siRNA) and thiol groups at the ω-end of PLL for coordinate bonding with AuNP. After confirming stable binding between single siRNA molecules and copolymers, the resulting uPICs were conjugated to a 20 nm AuNP to build uPIC-AuNP nanoarchitectures exhibiting sizes less than 50 nm and narrow size distributions under biological conditions. The uPIC-AuNPs achieved efficient siRNA accumulation in a subcutaneous tumor model by systemic administration and successfully induced sequence-specific gene silencing in the tumor tissue.

RESULTS AND DISCUSSION

Preparation and Characterizations of uPICs Comprising a Single PEG-PLL/siRNA Pair. PEG-PLL synthesis was targeted to possess 40 positive charges (or DP_{PLL} = 40), as it can complementarily neutralize the negative charges

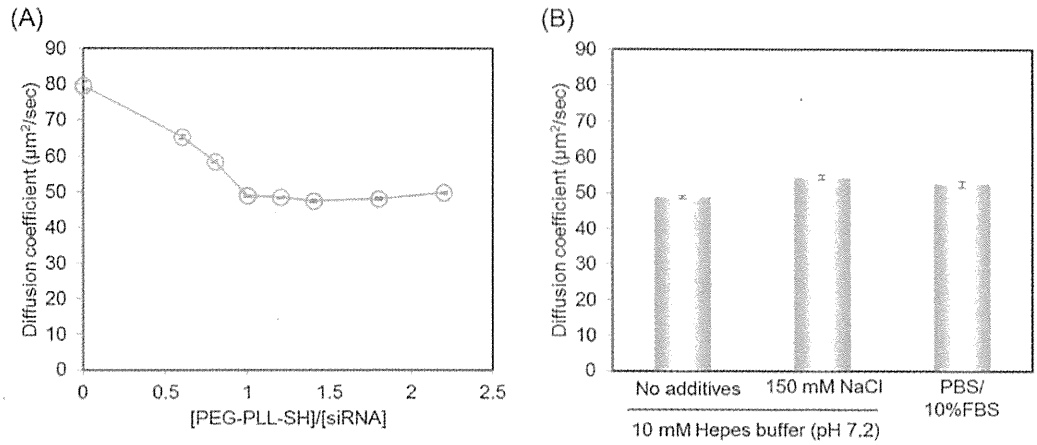

Figure 2. (A) Change in the diffusion coefficient of Cy3-siRNA upon polyionic complexation with PEG-PLL-SH in 10 mM Hepes buffer (pH 7.2) (Cy3-siRNA concentration = 10 nM). Results are expressed as mean and standard deviation (n = 10). (B) Diffusion coefficients of Cy3-siRNA-containing PICs prepared at [PEG-PLL-SH]/[siRNA] = 1.0 in various media (Cy3-siRNA concentration = 10 nM). Results are expressed as mean and standard deviation (n = 10).

of single 21mer/21mer siRNA and form uPICs through charge-matched polyionic complexation (Figure 1). The obtained PEG-PLL with TFA protective groups (PEG-PLL(TFA)) was determined to possess the DP_{PLL} of 38 in ^{1}H NMR spectrum (data not shown). The primary amine in the ω-end of PEG-PLL(TFA) was further modified with LC-SPDP for thiol-gold coordinate bonding, and the quantitative introduction of LC-SPDP was confirmed in ^{1}H NMR spectrum (Figure S1, Supporting Information (SI)). After successive removals of TFA and pyridyl groups with sodium hydroxide and dithiothreitol (DTT), respectively, the thiolated PEG-PLL (PEG-PLL-SH) was mixed with Cy3-labeled siRNA (Cy3-siRNA) at varying mixing ratios in 10 mM Hepes buffer (pH 7.2), and then characterized by fluorescence correlation spectroscopy (FCS). Note that FCS can determine a diffusion coefficient (D) of highly dilute fluorescent molecules even in serum-containing media.[21,22] The D values of PEG-PLL-SH/Cy3-siRNA mixtures decreased progressively with a molar ratio of PEG-PLL-SH to siRNA ([PEG-PLL-SH]/[siRNA]) and leveled off at [PEG-PLL-SH]/[siRNA] = 1 (Figure 2A). The initial decrease in the D indicates PIC formation between Cy3-siRNA and PEG-PLL-SH. The following plateau region in the D strongly suggests that all the Cy3-siRNAs were complexed with PEG-PLL-SH at [PEG-PLL-SH]/[siRNA] = 1, and an excess amount of PEG-PLL-SH at [PEG-PLL-SH]/[siRNA] > 1 did not bind to siRNA. The PIC prepared at [PEG-PLL-SH]/[siRNA] = 1 was further characterized by analytical ultracentrifugation (AUC) based on the absorbance at 260 nm for a precise structural determination. The molecular weight (MW) of PICs in 10 mM Hepes buffer (pH 7.2) containing 150 mM NaCl was calculated by combining the AUC (sedimentation equilibrium) data with a partial specific volume (PSV) of PICs (0.602 cm^3/g) and the buffer density (1.005 cm^3/g). Note that the PSV of PICs was determined as a mass average of PSV of siRNA (0.508 cm^3/g) and PSV of PEG-PLL (0.753 cm^3/g). The major parameters used for the calculation of MW of PICs are summarized in Table S1 (SI). The PIC exhibited a MW of approximately 22 kDa, consistent with the formation of a uPIC comprising a single pair of PEG-PLL (MW = 7200 Da) and siRNA (MW = 13 300 Da). Single siRNA loading in uPIC was confirmed by using FCS. The association number of siRNA in the PIC was determined to be 0.9 ± 0.1 using 10 nM Cy3-siRNA. It was calculated by normalizing the fluorescent particle number (or amplitude number particle) of the PIC to that of naked siRNA. Note that the diffusion coefficient of uPICs determined at 10 nM siRNA (~50 μm^2/sec) was maintained even at much higher concentrations, *i.e.*, 20 and 40 μM siRNA (Table S2 (SI)), indicating that the similar uPICs were also prepared under the preparation condition of uPIC-AuNPs (17 μM siRNA). The uPIC formation with a single pair of siRNA and PEG-PLL (DP of PLL = ~40) can be further validated from the standpoint of their molecular structures. Considering the fact that siRNA adopts a right-handed A-form helix with 11 bp per helical turn, a helical pitch of 2.8 nm, and a diameter of 2.3 nm,[23] PLL segment having the maximum main chain length of 4.1 nm per 11 amino acids and the maximum side chain length of 0.65 nm can completely make ion pairs with siRNA phosphates along the helical structure. Nevertheless, the complete ion pair formation between siRNA and PLL remains to be evidenced in further studies. The stability of uPICs prepared at [PEG-PLL-SH]/[siRNA] = 1 was further investigated by FCS (Figure 2B). The addition of 10% fetal bovine serum (FBS) and a physiological salt hardly affected the D values of the uPICs, indicating stable PIC formation under the biological conditions. These results demonstrated that the stable uPICs were selectively prepared using

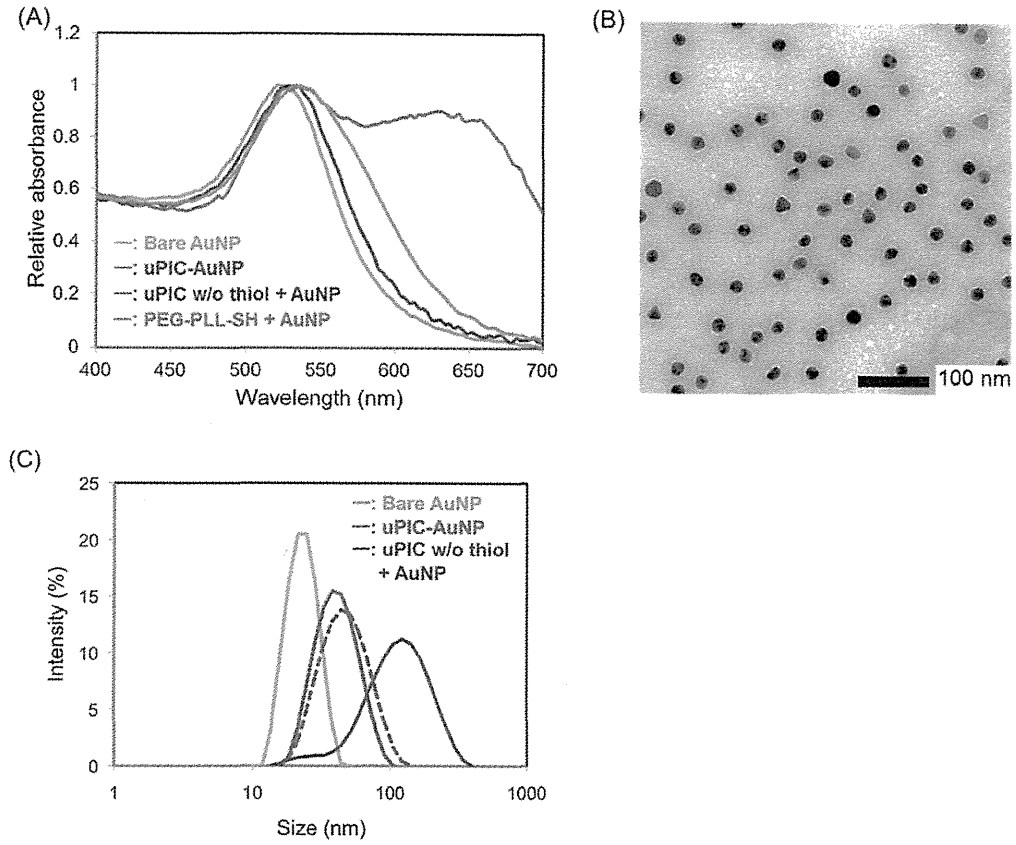

Figure 3. (A) UV–vis absorbance spectra of various sample solutions. Bare AuNP: AuNPs without PICs in 10 mM Hepes buffer (pH 7.2), uPIC-AuNP: uPIC-loaded AuNPs in 10 mM Hepes (pH 7.2) containing 150 mM NaCl, uPIC w/o thiol + AuNP: the mixture of AuNPs and uPICs prepared with nonthiolated PEG-PLL in 10 mM Hepes (pH 7.2) containing 150 mM NaCl, and PEG-PLL-SH + AuNP: the mixture of AuNPs and thiolated PEG-PLL without siRNA. (B) TEM image of uPIC-AuNPs. (C) Intensity-based DLS histograms of various sample solutions. Bare AuNP: AuNPs without PICs in 10 mM Hepes buffer (pH 7.2), uPIC-AuNP: uPIC-loaded AuNPs in 10 mM Hepes (pH 7.2) containing 150 mM NaCl (solid line) or 10% FBS (dashed line), and uPIC w/o thiol + AuNP: the mixture of AuNPs and uPICs prepared with nonthiolated PEG-PLL in 10 mM Hepes (pH 7.2) containing 150 mM NaCl. All samples were incubated overnight at ambient temperature (AuNP concentration: 12 nM).

PEG-PLL bearing ~40 positive charges, allowing their use as monodispersed building blocks for nanoconstruction.

Preparation and Characterizations of the Smart uPIC-AuNP Nanoarchitecture. uPICs were used as monodispersed building blocks for the construction of smart uPIC-AuNP nanoarchitectures (Figure 1). Specifically, the uPICs, which were prepared at [PEG-PLL-SH]/[siRNA] = 1 in 10 mM Hepes buffer (pH 7.2), were mixed with 20 nm AuNPs at a molar ratio ([siRNA]/[AuNP]) = 360 in the same buffer, then incubated at 4 °C for 8 h. Unbound uPICs were removed thoroughly by repeated centrifugal steps and the resulting uPIC-AuNPs were dispersed in 10 mM Hepes buffer (pH 7.2) containing 150 mM NaCl. The successful conjugation of uPICs onto AuNP was verified by UV–vis absorbance spectra, transmission electron microscopy (TEM), and dynamic light scattering (DLS). The absorbance spectrum of uPIC-AuNPs suggested that flocculation of AuNPs hardly occurred during the conjugation process, as a notable change in the absorbance spectra based on the surface plasmon resonance was not observed between bare AuNPs and uPIC-AuNPs (Figure 3A). Furthermore, the TEM image depicted that the uPIC-AuNPs were composed of single AuNP without particle aggregation, as their spherical shapes with a narrow size distribution (Figure 3B) were similar to those of the bare AuNP templates (Figure S2 (SI)). On the other hand, the intensity-based DLS histograms clearly show an increase in size of AuNPs after uPIC conjugation (Figure 3C). The peak top in the histogram was shifted from *ca.* 23 nm in bare AuNPs to *ca.* 38 nm in uPIC-AuNPs. Considering that the siRNA length is *ca.* 6 nm[24] and a hydrodynamic radius of PEG (MW = 2200) in a random coil is *ca.* 1.5 nm,[25] this size increase is consistent with the conjugation of uPICs on AuNP, as illustrated in Figure 1B. In addition, the zeta-potential of uPIC-AuNPs was determined to be −24.7 ± 0.4 mV. This value was significantly higher in the positive direction than that of bare AuNPs (−31.3 ± 1.2 mV), consistent with the presence of PEG outer shell in uPIC-AuNPs. It should be noted that the uPIC-AuNPs maintained their